HYDRODYNAMIC INVESTIGATION OF AN INNOVATIVE FLOATING PLATFORM FOR OFFSHORE WIND TURBINES

A Thesis Submitted to
the Graduate School of Engineering and Sciences of
İzmir Institute of Technology
in Partial Fulfillment of the Requirements for the Degree of

MASTER OF SCIENCE

in Civil Engineering

by
Elif GİRGİN

December 2022
İZMİR

ACKNOWLEDGMENTS

Firstly, I would like to thank Assoc. Prof. Dr. Bergüzar Özbahçeci for guiding me and believing in me with patience during my thesis. Also, I am grateful for allowing me to improve myself by including me in Tubitak 1001 and 1002 projects during my graduate education. Besides, I would like to thank her for allowing me to present some of the results of our study at the "Türkiye İnşaat Mühendisliği 18. Teknik Kongre ve Sergisi" held in Istanbul in November 2022.

Also, I would like to thank Assoc. Prof. Dr. Ünver Özkol for enabling me to participate in this special project.

This study was funded by the Scientific and Technological Research Council of Turkey,TÜBİTAK) under grants 217M451 and 121M933.

I want to express my sincere thanks to Ruwad Adnan Al Kareem for teaching me the ANSYS-AQWA program and guiding me with my numerical work whenever I got lost. Also, I would like to thank Kadir Aktaş and Salih Ak, who helped me through the experimental work.

I would also like to thank Gürkan Türkarslan for supporting me in every problem I have had and for always being there for me.

Finally, I would like to express my gratitude to my parents, Mediha Girgin and İlker Girgin, and my brother Mazlum Emre Girgin, for their endless support and faith.

ABSTRACT

HYDRODYNAMIC INVESTIGATION OF AN INNOVATIVE FLOATING PLATFORM FOR OFFSHORE WIND TURBINES

With the realization of the potential of wind energy in deep water, interest in floating platforms is increasing. In this study, the hydrodynamic behavior of offshore floating wind turbines was examined experimentally and numerically. This study is the first small-scale experimental model study on floating offshore wind turbines in Turkey. Experiments were carried out in the wave channel with dimensions of 40.0m×1.0m×1.4m in the hydraulic laboratory of the IZTECH Civil Engineering Department. A new floating platform developed through a Tübitak project was tested under various wave and extreme wind conditions. Responses of the turbine and platform system and the tensions in the mooring chains were measured. Free decay, hydrostatic, quasi-static, and regular and irregular wave and wind tests were performed. Results were compared with the results of the existing spar platform model tests under the same test conditions. It was concluded that the innovative platform was more stable than the spar platform, especially in terms of rotation in the y direction, which is critical for stable energy generation and fatigue loads. The new platform, together with the turbine and the mooring lines, was also modeled numerically using a potential theory-based program. Experimental free decay tests were used to calibrate the numerical model. After calibration, regular and irregular wave test results were used for the validation. Agreement between the numerical and experimental model studies showed that the numerical model of the innovative floating platform was verified and could be used to develop and examine the platform on a prototype scale.

ÖZET

AÇIK DENİZ RÜZGAR TÜRBİNLERİ İÇİN İNOVATİF YÜZER PLATFORMUN HİDRODİNAMİK AÇIDAN İNCELENMESİ

Rüzgar enerjisinin açıkdenizlerdeki potansiyelinin fark edilmesiyle yüzer platformlara olan ilgi artmaktadır. Bu çalışmada, deniz üstü yüzer rüzgar türbinlerinin hidrodinamik davranışı deneysel ve sayısal olarak incelenmiştir. Bu çalışma, Türkiye'de deniz üstü yüzer rüzgar türbinleri üzerine yapılan ilk küçük ölçekli deneysel model çalışmasıdır. Deneyler İYTE İnşaat Mühendisliği Bölümü hidrolik laboratuvarında bulunan 40.0×1.0m×1.4m ölçülerindeki dalga kanalında yapılmıştır. Tübitak projesi kapsamında geliştirilen yeni yüzer platform, çeşitli dalgalar ve aşırı rüzgar koşulu altında test edilmiştir. Türbin ve platform sisteminin tepkileri ve bağlama zincirlerindeki gerilimler ölçülmüştür. Serbest salınım, hidrostatik, yarı statik, düzenli ve düzensiz dalga ve rüzgar testleri yapılmıştır. Sonuçlar, aynı test koşulları altında mevcut spar platformunun sonuçlarıyla karşılaştırılmıştır. Özellikle kararlı enerji üretimi ve yorulma yükleri için kritik olan Y yönünde dönme açısından orijinal platformun spar platformuna göre daha stabil olduğu sonucuna varılmıştır. Yeni platform, türbin ve bağlama halatları ile birlikte potansiyel teori tabanlı bir program kullanılarak sayısal olarak modellenmiştir. Sayısal modeli kalibre etmek için deneysel serbest salınım testleri kullanılmıştır. Kalibrasyondan sonra düzenli ve düzensiz dalga testi sonuçları kullanılarak doğruşama yapılmıştır. Sayısal ve deneysel model çalışması arasındaki uyum, yeni yüzer platformun sayısal modelinin doğrulandığını ve sayısal modelin platformu prototip ölçeğinde geliştirmek ve incelemek için kullanılabileceğini göstermektedir.

TABLE OF CONTENTS

LIST OF FIGURES

Figure **Page**

Figure **Page**

Figure **Page**

LIST OF TABLES

Table **Page**

CHAPTER 1

INTRODUCTION

1.1. Research Background and Problem Statement

Currently, 79% of the energy demand is supplied by fossil fuels (United States Renewable Energy Fact Sheet, 2022). However, fossil fuels cause global warming by causing greenhouse gas accumulation in the atmosphere. The usage of fossil fuels has decreased, and the migration to renewable energy (solar, wind, geothermal, hydraulic, biomass, ocean energy, hydrogen, and storage) has started for this reason. Because of its great potential, wind energy is also the most popular kind of renewable energy. Wind turbines, which were first installed on land, were later installed in the sea. Up to 50 meters of water depth, fixed platforms have been used, but as the depth increases, floating platforms are preferred since they are less expensive than fixed platforms. The installation of a wind turbine in deep water offers several benefits. As the sea depth increases, the turbine moves away from the coast, and the elements that obstruct wind flow are eliminated, resulting in less turbulent winds. This increases the wind efficiency. As a result of the low surface roughness, high wind speed is an additional factor that will improve energy efficiency. Lastly, wind turbines installed on land and in shallow water might be aesthetically and audibly unpleasant to residents. In deep waters, these issues disappear. Floating platforms should maintain their balance in the face of environmental forces such as waves, winds, and currents to ensure that the vertical or horizontal axis wind turbines installed on them continue to operate effectively. Mooring cables connect the floating platform to the seabed, allowing for six degrees of freedom of movement. Currently, Spar, TLP (Tension Leg Platform), semi-submerged, and barge platforms are the most popular types of floating platforms. However, each one has disadvantages. For instance, the Spar type of platform has a high response to pitch motion, whereas the semi-submersible platform has a high response to heave motion. Because of the large cut-water plane area of the barge-type platform, wave interaction is high, and the cable cost increases as the depth at which the TLP will be placed increases, making it difficult to implement.

1.2. Aim and Scope of the Study

Floating platforms are the most critical component of a floating wind turbine, both in terms of performance and cost. 34% of the total cost of a floating wind turbine, is the cost of the floating platform and its connections, while only 22% is the cost of the turbine itself (Mone et al., 2017). As stated in the preceding section, the disadvantages of each type of platform indicate that the worldwide search for a more cost-effective and stable floating platform continues. A new platform was developed by the IZTECH team through a Tübitak project (Özkol et al., 2022, 217M451).

The purpose of this study is to conduct extensive hydraulic model tests to evaluate the hydrodynamic performance of the new floating platform with the turbine under regular and irregular wave and wind conditions. Experimental results were compared with results of a spar-type floating platform tested under the same wave and wind conditions. Moreover, a hydrodynamic model is developed, and the experimental results of the novel floating platform were used for the calibration and validation of the numerical model.

1.3. The Structure of the Thesis

This thesis is structured as follows: Chapter 2 provides an overview of the relevant academic literature. In chapter 3, the design of an innovative platform, the experimental set-up, and the numerical set-up are given. In chapter 4, the experimental results are given, including a comparison of the spar and the innovative platform. In chapter 5, the numerical model is calibrated and validated. Then, this thesis concludes with the study's key findings and a discussion of future research.

CHAPTER 2

LITERATURE REVIEW

2.1. General Review of offshore wind turbines

Offshore wind technology has been making rapid progress over the past 10 years. With the installation of 21,1 GW of offshore wind turbines to the grid in 2021, the total worldwide offshore wind capacity has increased to 57,2 GW (GWEC, 2022).

The offshore wind potential is encouraging the wind industry to migrate from land-based to offshore wind farms. As the industry evolves, offshore wind farms are built to achieve a stronger wind source in deeper offshore areas, revealing huge potential for the floating wind turbine market (DNV-GL, 2018). Current offshore wind energy market forecasts predict that 1400 GW of installed capacity will be reached worldwide in the next 30 years (OREAC, 2018). However, to determine their technical and economic feasibility, dynamic models are needed that consider the wind turbine, aerodynamics, elasticity, and controls of the wind turbine, as well as incident waves, sea currents, hydrodynamics, and platform and mooring dynamics of the buoyant (Jonkman, 2007).

2.2. Floating platforms

Floating platforms, which are designed to ensure the stability of floating wind turbines on the surface of the water, are one of the most essential structural components of a floating wind turbine system. In the past 10 to 15 years, various kinds of platforms for floating wind turbines have been developed; however, several typical platform geometries have arisen. As shown in Figure 2.1, these can be categorized into four broad categories: i) semi-submersible; ii) barge; iii) spar; and iv) TLP. To provide stability, these floating platforms employ passive stability methods such as ballast, buoyancy, and tensioned mooring lines.

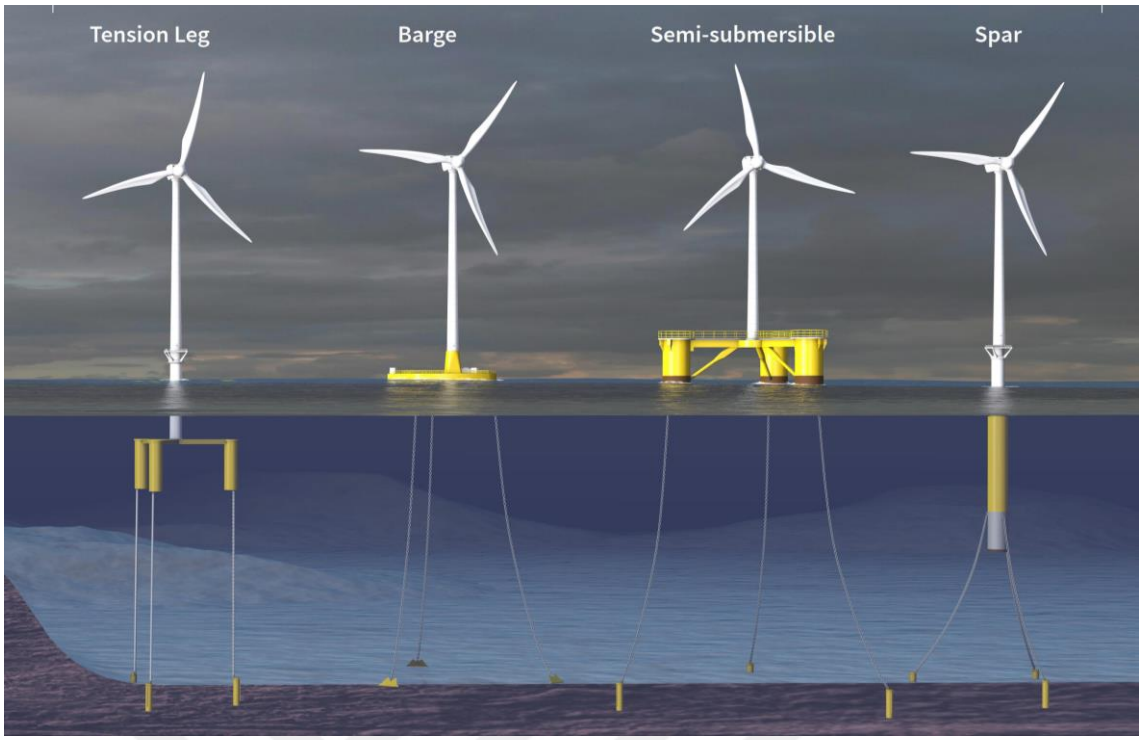

Figure 2.1: Conceptual floating offshore wind turbine concepts (Source: Crowle and Thies, 2021)

By adding weight at high drafts, the floating platform's rotational restorability is increased using the ballast method. (Jonkman, 2010). In the buoyancy method, restorations result from the disruption of the balanced buoyant force as the platform moves and the water-plane area increases. (Jonkman, 2007). In the tensioned mooring lines method, highly tensioned mooring cables provide restorations when any deviation from the original position of the platform occurs (Jonkman and Matha, 2013).

Barge platform employs the buoyancy method, Spar-buoy mainly employs the ballast method, and tension leg platform (TLP) primarily use the mooring tension method. Semi-submersible platforms often employ buoyancy as a major source of balance and ballast as their secondary method. (Figure 2.2).

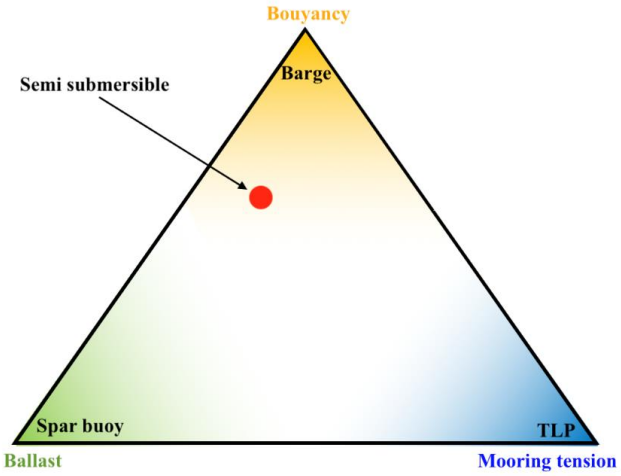

Figure 2.2: Stability triangle for floating platforms (Source: Butterfield et al., 2005)

Butterfield et al. (2007) evaluated the engineering difficulties of offshore floating platform systems for wind turbines. In this study, the relative advantages and disadvantages of different platform systems have been compared to each other, especially in order to ensure consistent stability. Musical et al. (2004) studied the applicability of floating platform systems to wind turbines and questioned the comparative assessment of several mooring methods in their research. Jonkman has conducted a detailed study on the dynamics of floating platform wind turbines (2009). In this work, several types of floating platforms are combined with various mooring systems, and aero-hydro-servo-elasticity is optimized. In this research, loads on wind turbine components such as the tower, nacelle, and gearbox were also examined under sea conditions.

2.3. Experimental Modeling of Floating Offshore Wind Turbine

In order to investigate the aerodynamics and hydrodynamics of an offshore floating platform, it is crucial to conduct scaled-down model tests. In addition to providing a trustworthy source for validating numerical tools, model tests can capture dynamic phenomena too (Li et al., 2018). A short overview of previous floating wind turbine (FWT) model experiments is provided. A prototype spar FWT with a 2 MW wind turbine was tested at different scales by Utsunomiya et al. (2009a, 2009b, 2010) at Kyoto University. These studies ranged in scale from a model basin test at 1:100 to a model sea test at 1:10. After several studies, the researchers determined that spar-type FWTs could

be a more affordable option for the offshore wind sector. However, in that study, wind and wave loads were not fully included in all the tests.

Also, a 1/20 scale model of the barge-type FOWT prototype was used for hydraulic model testing in the large flume (300 m × 5 m × 5 m) at Tainan Hydraulics Laboratory (THL) to determine the viability of the concept (Figure 2.3). The pitch and roll motions were confirmed to be compliant with the DNV standard by Yang et al. (Yang et al. 2022). Cermelli et al. (2010) performed model testing of the WindFloat offshore floating wind turbine with a semi-submerged platform system. In this experiment, aerodynamic and hydrodynamic forces are applied to the structure. In addition, the entire structure was examined in coupled mode during time-based analyses. The participants in the OC5 project modeled the aerodynamic, hydrodynamic, and mooring connections of the system using a variety of methodologies. In the following stage, participants' results were compared to an experiment conducted at the Maritime Research Institute of Netherlands (MARIN) in 2013 based on the DeepCwind FOWT model. The test model was performed on a performance-matching scale, a Marin Stock wind turbine (MSWT) (Kimball et al., 2014). As a consequence of this study, the performance of computer-aided engineering tools under different load conditions was analyzed and compared, and conclusions were drawn about how these tools can be improved.

Figure 2.3: OC5-DeepCwind model in the MARIN offshore basin (Source: Helder and Pietersma, 2013)

2.4. Numerical Modelling of FOWT

The physics behind the dynamics of FOWT systems are multi-variable and interactive, necessitating the use of computer-aided engineering (CAE) techniques to properly predict the FOWT system's behavior (Jonkman and Buhl, 2005). Some researchers favor precise solutions, such as computational fluid dynamics (CFD)-based numerical models that solve Navier-Stokes equations to represent platform motions and forces. This methodology has been utilized by Benitz et al. (2015), Tran and Kim (2018), and many others. Other options include applying a strategy based on potential flow, or Morison's equation, to the hydrodynamic sub-model and the Blade Element Momentum Theory (BEM) to the aerodynamic sub-model. On the other hand, custom algorithms can produce extremely rapid results. But it lacks the viscous effects that can be important in some situations.

While potential flow theory disregards viscous-induced excitation/damping, Morison's approach cannot be applied to structures with large diffraction. ANSYS™ AQWA® is a popular tool that uses both potential flow and Morison's equation (ANSYS Inc., 2013). As another tool OpenFAST, developed by Jonkman (2009), is a framework for fully coupled time-domain modeling of FOWTs by coupling numerical programs that represent aerodynamics, hydrodynamics for offshore structures, control and servo dynamics, and structural dynamics. The coupling framework, FAST2AQWA (F2A), was developed by Yang et al. (2020). F2A is a better numerical tool for forecasting the nonlinearities of a FOWT subjected to wind, wave, and current loadings. Since it combines the capabilities of two well-known analytical tools via a dynamic link library.

The International Energy Agency (IEA) has launched three studies (OC3, OC4, and OC5) to investigate and evaluate the soundness of several modeling methods. Phase IV of the Offshore Code Comparison Collaboration (OC3) project, which started in 2004 and was completed in 2009, is the first part (IEA Task 23, Subtask 3) (Jonkman and Musial, 2010). The second part (IEA Task 30) of the Offshore Code Comparison Collaboration Continuation (OC4) project was announced in 2010. OC3 and OC4 studies were conducted in order to compare, validate, and improve different numerical simulation tools.

In the first phase of the project, work was carried out on the OC3-Hywind Spar platform, but a semi-submersible platform was preferred in the OC4 phase, which can support an NREL 5-MW wind turbine. In the OC3 and OC4 phases, these platforms were subjected to various loading conditions and subsequently verified by code-to-code comparisons.

In order to clarify some of the discrepancies observed between simulation models in the OC4 phase, the Offshore Code Comparison, Continued, with Correlation (OC5) phase was initiated in 2014, which compared simulations and the results of physical model experiments (Figure 2.4). In this study, the model of a semi-submersible platform was compared to both the OC4 simulation and the OC5 physical experiment results (Robertson, 2015).

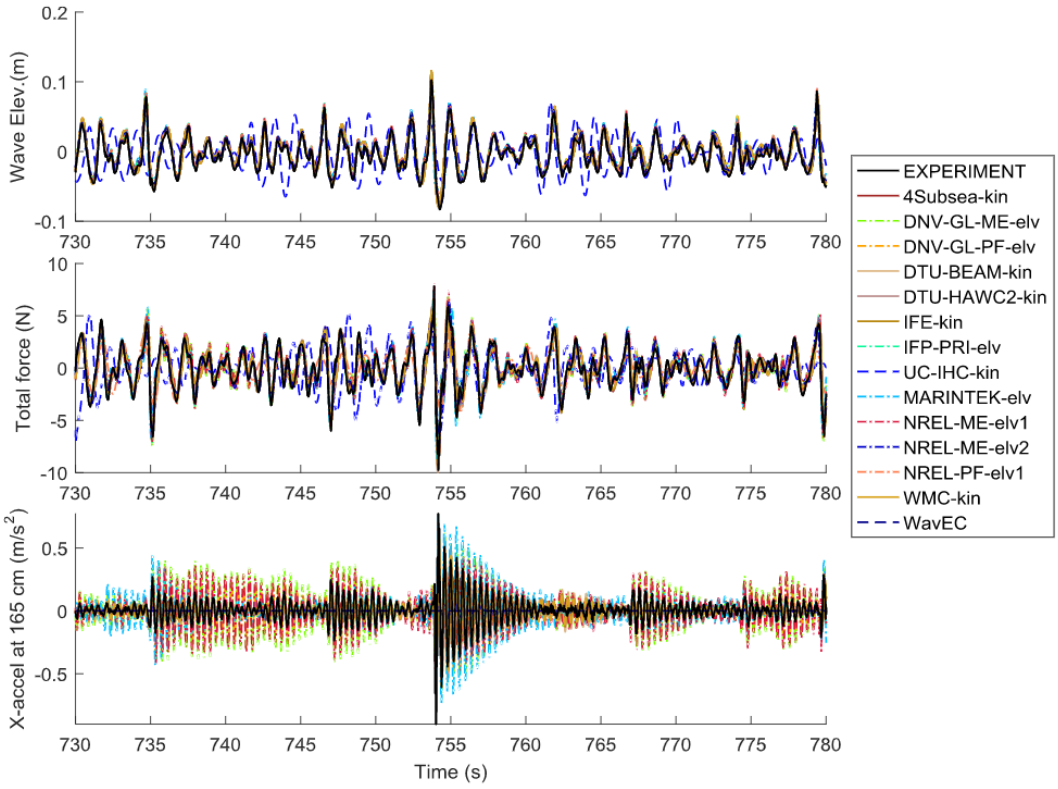

Figure 2.4: Validation of simulation responses against experimental measurements (Source: Robertson, 2016)

CHAPTER 3

RESEARCH METHODOLOGY

3.1. Innovative Floating Platform Design

The floating platform is the most crucial structure for the system's integrity and stability in offshore floating wind turbines. Although there are various kinds of floating platforms, such as spar, TLP, and semi-submersible, the search for a more stable and economical floating platform continues to reduce hydrodynamic and aerodynamic responses. For this reason, a new platform has been designed to provide an innovative alternative to the offshore floating turbine platforms currently available on the market. The platform is designed to support a 5 MW wind turbine. Although there are other varieties of turbines in terms of power, 5 MW was chosen since it is a reference turbine, and it is easier to obtain the required technical information about the turbine. In the early stages of the design, a hybrid design was planned by considering the advantages and disadvantages of existing floating platforms. Figure 3.1 shows the initial version of the floating platform developed by combining of spar and semi-submersible platforms.

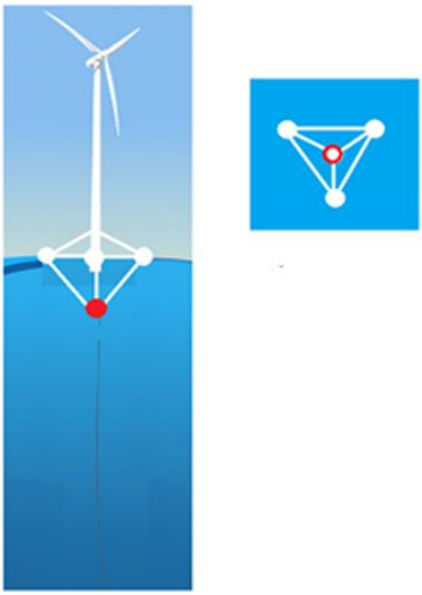

Figure 3.1: Initial version of the innovative floating platform (Source: Özkol et al., 2022)

The initial design of the platform consists mainly of three floaters and the ballast. These three floaters, the ballast, and the tower are connected by steel pipes. In this design, similar to semi-submersible platforms, the water-plane area is low and distributed to the wider area to increase the rotational stiffnesses and, therefore, to enhance the roll and pitch responses. As it is in the spar platforms, the ballast increases the metacentric distance by lowering the center of gravity, hence contributing to the platform's stability. The use of ballast as a counterweight at the bottom also contributes to lowering the structure's cost without increasing the draft.

Following this initial design, the platform was modified during two Tübitak projects (Özkol et al., 2022, 217M451; and Özbahçeci et al., 2022, 121M933). One of the modifications was that the floaters positioned on the surface of the water were pulled below the water level. It means that they were submerged. This is because it reduces the impact of wave motions on the structure which has a larger effect on the water surface. The adoption of steel chains instead of steel pipes to connect the platform elements is another improvement. It is expected that this will contribute positively to the structure in terms of cost, flexibility, and practicality. In addition, it is expected that the use of concrete instead of steel for the floaters will keep costs down.

After the conceptual design was completed, a more detailed optimization phase was initiated. In the optimization study, 800 different alternatives were examined by changing the parameters between the lower and upper limit values given in Table 3.1 to achieve an optimal design in terms of stability and cost.

Table 3.1: Parameters and their ranges used in the optimization study

Parameter	Lower limit	Upper limit
Number of floaters	3	6
The angle of the floater arm with the vertical axis (degrees)	15	30
Outermost diameter of the platform (m)	20	40
Volume of floaters (m^3)	1000	3375
Chain diameter (for connection to the base and all elements to each other) (mm)	60	100

During the optimization study, the following criteria are required for a successful platform candidate:

- Hydrostatic stability should be ensured,
- Metacenter distance > 0 (> 1m, DNVGL-ST-0119)
- Wind heeling moment < 6˚ (for the operation), < 12˚ (for the survival mode) (DNVGL-OS-C301).

To enhance the efficiency of a floating wind turbine, it is necessary to reduce nacelle acceleration caused by platform pitch and surge motion. This motion imposes additional loads on the wind turbine blades, increases drivetrain strain, and shortens the system's lifespan (Sclavounos et al. 2010). Therefore, keeping the maximum wind rotation angle as low as possible is advantageous for the structure.

- Factor of safety for the mooring chains > 1.27

The ratio of the maximum stress in the chain to the maximum load it can carry, known as the chain's breaking rupture safety, is determined to be at least 1.27 (DNVGL-OS-C301). This rate was computed by considering the decrease in chain diameter caused by corrosion after 20 years.

- Total cost of the platform < 9 million $.

A cost restriction is added to the optimization issue to avoid expensive design configurations. This inequality constraint limited the platform's price to less than $9 million (Karimi et al. 2016).

In the optimization study, firstly, simple mathematical calculations were conducted to estimate the hydrostatic response of the system and platform cost. The two objectives of optimization were cost and the wind heeling moment of the system, which is defined as the rotational response under constant wind excitation at rated wind speed that induces maximum thrust force. 800 alternatives were reduced to 36 via the Pareto front method after all these conditions were examined. Figure 3.2 demonstrates the comparison of the alternatives in terms of the wind heeling moment and the cost. In Figure 3.2, the maximum wind heeling moment is 2 °, and the cost is $9 million.

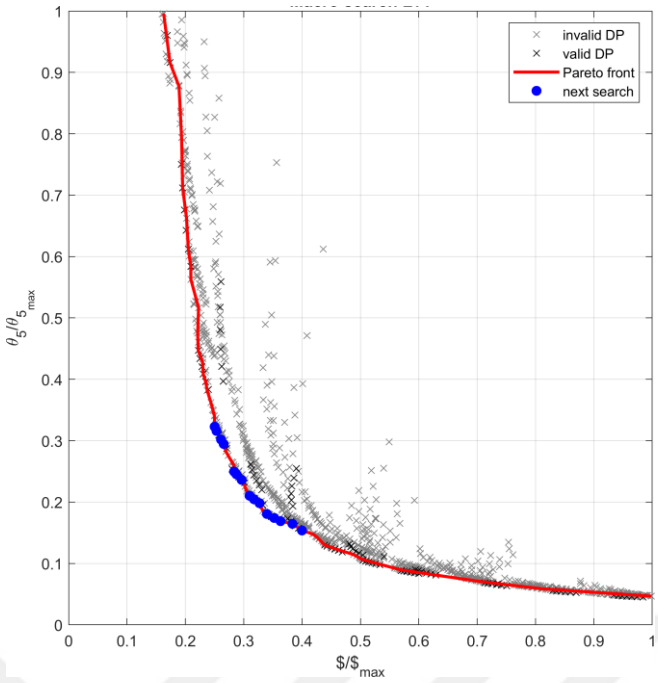

Figure 3.2: Pareto front analysis of innovative floating platform (Source: Özkol et al., 2022)

As shown in Figure 3.2, the cost increases as the wind heeling moment decreases, which increases the stability. While some alternatives were invalid due to their inability to meet the required criteria given above, a Pareto facade was constructed for the valid alternatives, and those that provided the minimum values for both wind heeling moment and cost were chosen; these were the alternatives that promoted to the second stage of the optimization analysis.

In the second phase, hydrodynamic diffraction analyses were conducted using ANSYS-AQWA to identify among the 36 remaining alternatives for the novel model to choose the most optimal. In the second stage, in addition to the structure's cost and wind rotation angle, the displacement in the x and z direction and the rotational motion in the y direction were included. In hydrodynamic diffraction analysis, the response amplitude operator (RAO) of the structure was compared in the frequency domain without mooring cables. The optimization study ended with hydrodynamic response analyses in the time-domain including the mooring cables.

In order to improve the response of alternative platforms on the z-axis, the diameter of the floaters was increased while their height was decreased to remain the same volume. In addition, it was decided to suspend heave plates on the chains connecting the platform's components. Thus, it is aimed to decrease the response by increasing the stability in the z direction. The platform that emerged because of the analyses and improvements is shown in Figure 3.3.

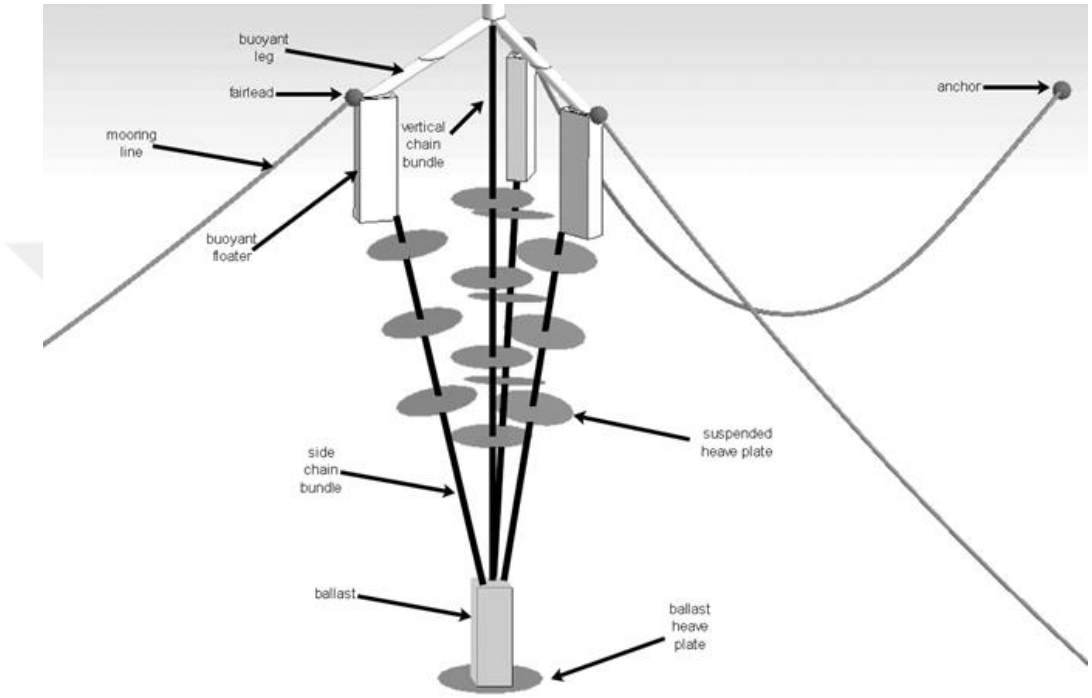

Figure 3.3: Novel platform design for 5 MW wind turbine and 200-m water depth (Source: Özkol et al., 2022)

As a result of all this optimization analysis, a unique floating platform has been developed, which is both low in cost and has a good performance especially in motions that are critical for the stability of wind turbines such as heave and pitch and to produce energy. As shown in Figure 3.3, the new platform consists of three floaters, floater arms, chains, and heave plates suspended on the chains. The floaters were spread over a large area, resulting in a low-pitched response. Since the floaters were below the water level, only a section of the floaters' arms remained in contact with the water's surface. Therefore, the platform was protected from the effect of waves. To reduce the high heave motion that existed in the initial design, heave plates were added subsequently.

The characteristics of the innovative floating platform designed for a 5MW wind turbine are given in Table 3.2

Table 3.2: Novel platform properties for 5MW wind turbine

Overall System Properties	
Water depth (m)	200
Total draft (m)	190.09
Freeboard (m)	10
Mass (total system) (ton)	6326.3
CG below SWL (total system) (m)	-59.82

Platform Topology	
Buoyant floaters	
Number of buoyant floaters/legs	3
Angle of buoyant legs in the vertical plane (deg)	30.00
Outermost radius of the platform (m)	39.26
Depth to top of buoyant floaters below SWL (m)	9.49
Depth to bottom of buoyant floaters below SWL (m)	41.64
Width of buoyant floater (m)	5.51
Length of Buoyant floater (m)	11.02
Wall thickness of buoyant floater (mm)	300
Diameter of buoyant legs (m)	3.51
Length of buoyant legs (m)	38.97
Wall thickness of Buoyant leg (mm)	87.77
Ballast	
Ballast mass in air (ton)	1342.68
Ballast mass in water (ton)	1170.65
Ballast CG below SWL (m)	187.50
Ballast diameter (m)	6.54
Ballast height (m)	5.00

(cont. on next page)

(table cont.)

Chain bundles	
Number of middle chain bundles	4
Nominal diameter of middle chains (mm)	90.00
Number of chains in the bundle	2
Bundle air mass per unit length (kg/m)	322.38
Length of vertical bundle (m)	195.00
Length of side bundle (m)	147.28
Heave plates	
Number of vertically suspended heave plates	2
Number of side suspended heave plates	3
Number of ballast heave plates	1
Diameter of suspended heave plate (m)	18.48
Diameter of ballast heave plate (m)	18.48
Thickness of heave plates (mm)	87.80
Air mass of a suspended heave plate (ton)	188.47
Air mass of a ballast heave plate (ton)	188.47
Mooring System Properties	
Mooring cross-sectional properties	
Number of sections	1
Line Type	R3 studless Mooring chain
Nominal diameter (mm)	90
Dry mass/unit length (kg/m)	161.19
Equivalent diameter (mm)	162.00
Stiffness: EA (kN)	691740.00
maximum breaking strength (kN)	6623.25

(cont. on next page)

(table cont.)

Mooring configuration	
Mooring system type	Chain catenary
Number of mooring lines	3
Angle between adjacent lines on the horizontal plane (deg)	120
Depth to anchor below SWL (m)	200
Depth to fairleads below SWL (m)	9.49
Radius to anchors from platform centerline (m)	658.43
Radius to fairleads from platform centerline (m)	39.26
Mooring line pretension (kN)	1192.81
Unstretched mooring line length (m)	663.70

3.2. ANSYS-AQWA Model

The FOWT system was assumed to be rigid, and the software ANSYS™ AQWA® was used to simulate the system's hydrodynamics and anchoring dynamics. The right-hand axis rule was used throughout the entire study, whereas the positive z-axis depicts the upward. Two origins are specified within the system: the point where the tower centerline coincides with still water (O) and the undisplaced center of gravity (O') of the system.

The platform's motion comprises six degrees of freedom, which include displacement (surge X, sway Y, heave Z) and rotation (roll RX, pitch RY, yaw RZ) (Figure 3.4). Heave, roll, and pitch motions can be restored naturally under the influence of gravity; however, surge, sway, and yaw motions cannot. In this study, motions in the directions of surge, heave, and pitch were analyzed.

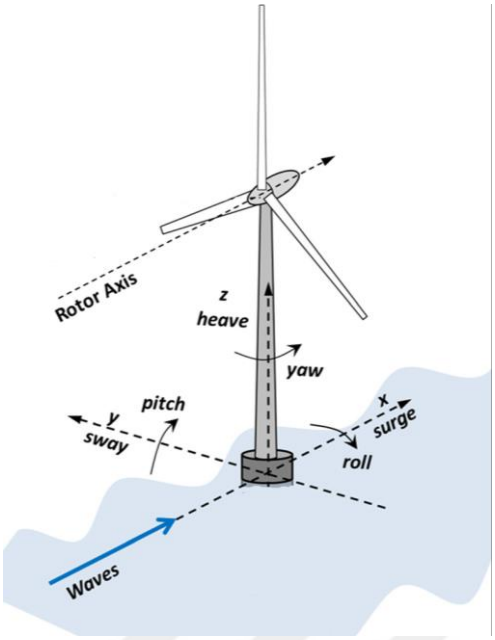

Figure 3.4: 6 DoF for a floating platform (Source: Sant&Cuschieri, 2016)

ANSYS™ AQWA® is a software that allows the investigation of the effects of environmental factors on floating and fixed offshore structures in the time and frequency domain. Given the huge number of potential combinations of environmental conditions, a time domain analysis would be too time-consuming for a systematic parametric investigation; however, a frequency domain assessment of the system response may provide a simple and quick method to meet this need (ANSYS Inc., 2013). General expressions (Eqs. 3.1 and 3.2) are provided for the time domain and frequency domain:

$$[-\omega^2 M - i\omega C + K]U = F(\omega) \tag{3.1}$$

$$M\ddot{U} = F(t) \tag{3.2}$$

where M, C, and K are the 6×6 matrix of structural mass, damping, and stiffness, U is the 6×1 matrix of motion response and F is the 6×1 matrix containing the combination of all external forces as a function of frequency ω or time t. Also, displacement stated as U and velocity stated as $\dot{U}$ matrices.

ANSYS™ AQWA® is capable of simulating first order (Airy wave) and second order (2nd order Stokes wave) regular water waves in deep and finite depth water. Moreover, the linear superposition method may be used to simulate unidirectional or multidirectional irregular waves. In accordance with the linearized Airy wave theory, regular waves are the most fundamental form of a monochromatic wave (constant wave height and period). Under the simplifying assumption that the flow is irrotational, and incompressible, the Laplace equation for an ideal fluid is used to get the surface profile solution. The surface wave elevation η is described as:

$$\eta(x,t) = a\cos(kx - \omega t + \epsilon_0) \tag{3.3}$$

where;

$$k = \frac{2\pi}{L};\ \ \omega = \frac{2\pi}{T} \tag{3.4}$$

Here, a is the wave amplitude, L is the wavelength, T is the wave period, k is the wavenumber, ω is the wave angular frequency, t is the time, x is the Cartesian coordinate in the horizontal axis, and ϵ_0 is the initial phase of the wave

This study defines irregular waves using the Joint North Sea Wave Project (JONSWAP) spectrum. The following Eq. (3.5 to 3.7) describes the spectrum $S(f)$ as a function of the significant wave height H_s and the spectral peak period T_p (Goda, 2010):

$$S(f) = \beta_{ij} H_s^2 T_p^{-4} \exp\left[-1.25\left(T_p f\right)^{-4}\right] \gamma^{\exp\left[-\frac{\left(T_p f - 1\right)^2}{2\sigma^2}\right]} \tag{3.5}$$

in which;

$$\beta_{ij} \cong \frac{0.0624\ (1.094 - 0.01915\ln\gamma)}{0.230 + 0.0336\,\gamma - 0.185(1.9+\gamma)^{-1}} \tag{3.6}$$

$$\gamma = 1\sim7, \qquad \sigma \cong \begin{cases} 0.07: & f \le f_p, \\ 0.09: & f > f_p. \end{cases} \tag{3.7}$$

where γ is the peak amplification factor. According to Hasselmann et al. (1973), its value varies between 1 and 7 with a mean of 3.30.

By adjusting, which affects the sharpness of the spectral peak, it is possible to obtain a spectrum of wave energy with various forms. Notably, H_s is the mean of the greatest one-third of wave heights in the wave train established by the zero-up crossing approach.

3.2.1. Boundary Conditions

3.2.1.1. Kinematic Free-surface Condition

By virtue of this boundary condition, particles traveling along the wave's free surface are required to travel at the same velocity as the surface itself. This condition can be stated technically as follows:

$$U|_{z=\eta} = U_n \tag{3.8}$$

where z is still water level, η is the wave surface profile, and n is the unit normal vector pointing away from the free surface (Hedberg and Sacculo, 2014).

3.2.1.2. Sea Floor Condition

Within this condition, the sea floor is considered a solid layer, with no border crossings permitted. McCormick (2010) formulates the sea-floor boundary condition as follows:

$$U.N|_{z=-h} = \frac{\partial \Phi}{\partial N}\Big|_{z=-h} \tag{3.9}$$

where h represents water depth, Φ represents velocity potential and N represents the normal unit vector to the seabed.

3.2.1.3. Dynamic Free-surface Condition

According to this boundary condition, the free-surface pressure gauge is zero at any time and at any location. Due to the velocity term being empowered by 2, the equation of this condition is non-linear. This condition can be formulated as:

$$\left\{ \frac{\partial \Phi}{\partial t} + \frac{U^2}{2} + g\eta \right\} \Big|_{z=\eta} = 0 \tag{3.10}$$

3.2.1.4. Linearized Free-surface Boundary Condition

The linearized free-surface condition is achieved by combining the dynamic free-surface boundary condition with the kinematic free-surface boundary condition at the vertical free-surface displacement.

$$\left\{ \frac{1}{g} \frac{\partial^2 \Phi}{\partial t^2} + \frac{\partial \Phi}{\partial z} + g\eta \right\} \Big|_{z=\eta \cong 0} = 0 \tag{3.11}$$

3.2.1.5. Body Boundary Condition

This condition prohibits any flow from passing through the hull's surface. It is assumed that the normal velocity of the fluid at the submerged section of the hull surface S_B is equal to the normal velocity of the floating part.

$$\frac{\partial \Phi}{\partial n} = \frac{\partial s}{\partial t} \cdot n \Big|_{S_b} \tag{3.12}$$

where s is the displacement vector of a point x.

3.2.1.6. Far-field Boundary Condition

This phenomenon depicts the progressive attenuation of a body's radiated waves as they move farther away from their source. Hence, it is stated that there are no radiated waves at an infinite distance from the body.

$$\lim_{r\to\infty}|U| = 0 \tag{3.13}$$

where r is the radial distance.

3.2.2. Hydrodynamic Model

3.2.2.1. First-Order Potential Theory

Active excited wave forces and reactive inertial forces are classified as wave-induced linear forces. The active forces consist of the direct incident wave force, also known as the Froude-Krylov force, which is unaffected by the presence of the body, and the diffraction force produced by the disruption in the wave caused by the presence of the body. Given the velocity potential term shown below, which defines the fluid flow field around the floating platform:

$$\Phi\left(\overrightarrow{X}, t\right) = a\,\varphi\left(\overrightarrow{X}\right)e^{-i\omega t} \tag{3.14}$$

The space-dependent velocity potential $\varphi\left(\overrightarrow{X}\right)$ is composed of contributions from the incident wave φ_1, diffraction wave φ_d, and the body motion-induced radiation forces $\varphi_{rj}. j = (1,3)$ denotes displacement, $j = (4,6)$ states rotational movements. Then $\varphi\left(\overrightarrow{X}\right)$ can be expressed as:

$$\varphi\left(\overrightarrow{X}\right)e^{-i\omega t} = \left[(\varphi_1 + \varphi_d) + \sum_{j=1}^{6}\varphi_{r_j}x_j\right]e^{-i\omega t} \tag{3.15}$$

Using the Bernoulli equation and the wave velocity potential, a first-order hydrodynamic pressure distribution can be obtained.

$$p^{(1)} = -\frac{\rho \partial \phi(\overrightarrow{X}, t)}{\partial t} = i\omega\rho\varphi(\overrightarrow{X})e^{-i\omega t} \tag{3.16}$$

Finally, AQWA-adopted total first-order hydrodynamic force mathematical model that can be is as follows:

$$F_j e^{-i\omega t} = -\int_{S_0} p^1 n_j dS = \left[-i\omega\rho \int_{S_0} \varphi(\overrightarrow{X})\, n_j dS\right] e^{-i\omega t} \tag{3.17}$$

where $(\overrightarrow{X}) = (x, y, z)$. The components of the total force in Eq. (3.17) are:

j^{th} Froude-Krylov force of the incident wave:

$$F_{1_j} = -i\omega\rho \int_{S_0} \varphi_1(\overrightarrow{X}) n_j dS, \tag{3.18}$$

the j^{th} diffracting force due to the diffraction wave:

$$F_{d_j} = -i\omega\rho \int_{S_0} \varphi_d(\overrightarrow{X}) n_j dS, \tag{3.19}$$

and the j^{th} reactive, radiation force due to the radiation wave caused by the k^{th} mode of motion:

$$F_{r_{jk}} = -i\omega\rho \int_{S_0} \varphi_{r_k}(\overrightarrow{X}) n_j dS \tag{3.20}$$

3.2.2.2. Second-Order Potential Theory

Second-order wave forces arising in irregular waters may be defined as the contribution of a pair of sinusoidal waves. Wave drift forces are the horizontal components of the second-order wave forces. Under the effect of these forces, an unrestrained floating vessel shows a steady and slow drift along the general direction of wave propagation. Suction forces are the vertical components of the second-order wave forces. This expression is commonly associated with the vertical force and pitching moment exerted on submarine vehicles while they are hovering or traveling near the

water surface (Pinkster, 1980). Second-order force in the time domain was defined by Pinkster, (1980), as the sum of the following five components:

$$\overrightarrow{F^{(2)}}(t) = \iint_{S_0} \left(\rho \frac{\partial \Phi^{(2)}}{\partial t}\right)\vec{n}dS + \oint_{WL} \left(-\frac{1}{2}\rho g\left(\eta^{(1)}\right)^2\right)\vec{n}dl + \frac{1}{2}\rho \iint_{S_0} \left|\nabla\Phi^{(1)}\right|^2 \vec{n}dS + \rho \iint_{S_0} \left(\vec{X}^{(1)} \cdot \frac{\nabla\partial\Phi^{(1)}}{\partial t}\right)\vec{n}dS + \vec{\alpha}^{(1)} \times \vec{F}^{(1)} \quad (3.21)$$

$\vec{\alpha}^{(1)}$ represents the linearized rotation matrix of the body's center of gravity.

This equation includes second-order potentials, first-order relative wave elevation, first-order pressure drop, and pressure due to the product of the gradient of first-order pressure and first-order motion, first-order angular motion, and inertial forces, respectively.

Considering pairs of sinusoidal waves with frequencies $(\omega_i; \omega_j)$ wave amplitudes $(a_i; a_j)$, and phase shifts $(\varepsilon_i; \varepsilon_j)$ to solve the second order wave forces in the frequency domain, Eq. (3.15) can be written as follows:

$$F_{i,j}^{(2)}(t) = Re\left\{\sum_i \sum_j a_i a_j QTF_{ij}(\omega_i; \omega_j) e^{-i[\omega_i - \omega_j]t + \varepsilon_i - \varepsilon_j}\right\} \quad (3.22)$$

where QTF (Quadratic Transfer Function) represents the quadratic transfer function. It is the amplitude of second-order force per unitary pair of wave amplitudes. The real part of QTF_{ij} specifies the i^{th}, j^{th}) amplitude of the second-order force per unitary pair of waves. When, $\omega_i = \omega_j$ the wave force is a constant mean drift force, and the difference in frequencies $\omega_i - \omega_j$ causes the slow-changing motions.

3.2.2.3. Morison's Equation

Another important factor is viscous force, which becomes vital for thin structures or when big waves are encountered. Using the ratio of a body's typical diameter (*D*) to its wavelength *(L)* is one technique to classify the types of impacts it gets. If this ratio is

smaller than 0.2, the dominance of diffraction forces decreases, and the importance of the drag force increases. The drag component operating on a unit length of a cylinder immersed in water is proportional to the square of the relative velocity between the body at that strip $\dot{u}_j$ and the wave-induced water particle q. For translational motion modes ($j = 1,2$), the Morison force is the sum of a drag component and an inertia component:

$$dF_M = \frac{1}{2}\rho_f D C_d \left|\dot{q} - \dot{u}_j\right|\left(\dot{q} - \dot{u}_j\right) + C_m \rho_f \frac{\pi D^2}{4}\ddot{q} - (C_m - 1)\rho A \ddot{u}_j \tag{3.23}$$

where $C_m = (1 + C_a)$ is the inertia coefficient and C_a is the added mass coefficient.

3.2.3. Mooring Model

3.2.3.1. Quasi-Static Model

A quasi-static model is typically employed during the early design phase, it neglects the hydrodynamic drag and inertia wave effects that occur on the cable. The force exerted by the mooring lines on the platform can be expressed as follows:

$$F_j^{lines} = F_j^{lines,0} - k_{jj_m} \cdot \dot{x}_j \tag{3.24}$$

$F_j^{lines,0}$ represents the net force of the mooring lines on the platform when the platform is in its original position. J.M. Jonkman developed the mathematical formulation of an elastic catenary line hanging in water between an anchor and a fairlead (2007). Using the following equations (origin at the anchor), the vertical and horizontal tensions at the fairlead ($T_H; T_V$) can be determined:

$$x_f(T_H, T_V) = L_c - \frac{T_V}{\omega} + \frac{T_H}{\omega}\sinh^{-1}\frac{T_V}{T_H} + \frac{T_H L_c}{EA} \tag{3.25}$$

$$z_f(T_H, T_V) = \frac{T_H}{\omega}\left[\sqrt{1 + \left(\frac{T_V}{T_H}\right)^2} - 1\right] + \frac{1}{2EA}\left(\frac{T_V^2}{\omega}\right) \tag{3.26}$$

where L_B is laid length and formulated as $L_B = L_c - T_V/\omega$, L_c is the cable's length. x_f and z_f refers to the horizontal and vertical coordinates of the fairlead position, EA is the axial stiffness of the mooring cable, and ω is its weight per unit length.

3.2.3.2. Dynamic Model

The dynamic model is utilized in time-dependent analyses that requires comprehensive research. The time-dependent hydrodynamic forces F_h can be expressed as:

$$F_h = F_B + F_d - m_a\left[\vec{a}_j, \vec{a}_{j+1}\right]^{\mathrm{T}} \tag{3.27}$$

where F_B is the buoyant force, F_d is drag force. Also, m_a represents the primary added mass, whereas $\vec{a}_j$ indicates the acceleration at the j^{th} node.

The seabed creates a force on the cable resting on the ground. Considering a node j has a position $\vec{R} = (x_j, y_j, z_j)$, the spring-like response force F_{zj} is described as follows:

$$F_{zj} = \begin{cases} 0, & z_j > h + \hat{z} \\ \dfrac{m'g}{\hat{z}}\left[d + z_j + \dfrac{\hat{z}}{pi}\sin - \dfrac{\pi\left(h + z_j\right)}{2\hat{z}}\right], & z_j \le h + \hat{z} \\ \dfrac{m'g}{\hat{z}}\left[\hat{z} + 2\left(h + z_j\right)\right], & z_j \le h \end{cases} \tag{3.28}$$

where m' is the net mass, including buoyancy.

3.2.4. Numerical Design of Innovative FOWT

The geometry of the platform that will carry the 300-kW wind turbine was initially modeled in Ansys SpaceClaim. Since three-dimensional radiation/diffraction panel analysis was adopted for hydrodynamic analysis, floater arms and floaters were defined as thin surface bodies with length and angle values suited to the model geometry. After this phase, the geometry was shared with the hydrodynamic diffraction and hydrodynamic response tools. With the hydrodynamic diffraction tool, the system's mass and center of

gravity were determined. In addition, heave plates, platform chains, and mooring cables were modeled. Properties of the mooring cables, such as length, chain diameter, and stiffness, were computed via a custom-written algorithm, and the mooring cables were represented as nonlinear catenaries. Following this step, the model's surface was divided into 10788 panels with a maximum size of 0.5 m. Figure 3.5 depicts the numerical model of the platform (left) and the mesh version of the same numerical model (right).

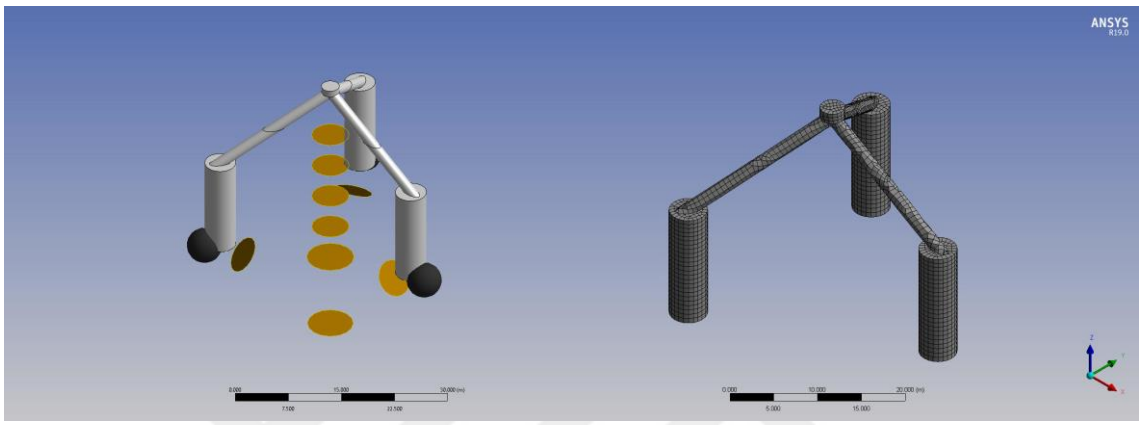

Figure 3.5: Innovative platform in ANSYS AQWA

In hydrodynamic diffraction, the input values were 40 m of water depth and 1 t/m3 for water density. The range of wave directions was 180°–180°, with a 90° interval. The frequency of the wave was fixed at an equal periodic interval. The interval range was 1.18 s, while the period range was 2.5–62.5 s. Following these procedures, the hydrodynamic response module was activated for analysis. This module allows for stability analysis, frequency-dependent analysis, and time-dependent analysis.

In the ANSYS-AQWA Hydrodynamic Diffraction module, several kinds of outputs are accessible, such as diffraction, Froude-Krylov, diffraction + Froude-Krylov, linearized tube drag, and total exciting force including tube drag; response amplitude operators (RAOs) and RAOs with linearized tube drag; radiation damping and added mass; steady drift; sum QTF and difference QTF; splitting forces; bending moment, and shear force. This tool basically illustrates how these forces, moments, or phase angles change with direction, frequency, or both direction and frequency.

In the ANSYS-AQWA hydrodynamic time response module, several graphs are accessible to monitor the behavior of a set of parameters over time, such as structure

position, structure velocity, structure acceleration, structure forces, fender forces, joint forces, joint forces, cable forces and time step error.

The state of hydrostatic equilibrium was determined via stability analysis. The floating platform was shifted in the (+*x*) and (-*x*) directions for quasi-static analysis, and cable tensions were analyzed using stability analysis. For the free decay tests, the responses of the platform were examined by applying displacement in the (+*x*) and (-*z*) directions and rotation in the (+*ry*) direction without the influence of wave and wind. For regular wave experiments, wave direction, experimental duration, wave amplitude, and wave period values were defined, and surge, heave, and pitch responses, as well as the tension forces of the cables, were assessed. Following the JONSWAP spectrum, wave direction, test duration, significant wave height, peak wave period, and gamma factor values were entered for irregular wave experiment tests, motion responses, and cable tensions examined. In addition to investigating regular and irregular waves, the effect of the wind was also studied. To achieve this, the wind speed profile is converted to wind force, and forces are applied to those points in the direction of the wind's arrival.

Throughout these modeling and analysis phases, meter "m" was selected as the unit of length, tonne "t" as the unit of mass, kilonewton "kN" as the unit of force, and degree "°" as the unit of angular values.

3.3. Experimental Set-up

3.3.1. Model Scale

The Froude and Reynolds numbers, respectively, can be used to scale hydrodynamic and aerodynamic forces. The Froude number is a ratio of inertial and gravitational forces; this dimensionless number indicates dynamic similarity. Typically, the Froude number is employed to quantify the surface wave forces generated by gravity.

$$Fr = \frac{U}{\sqrt{gL}} \tag{3.29}$$

U is the fluid velocity, *g* is the gravitational acceleration, and *L* is the characteristic length.

If the model scale is λ Scale factors of parameters according to Froude law are given in Table 3.3.

Table 3.3: Scale factors of parameters

Parameter	Unit	Scale Factor
Length	[L]	λ
Area	$[\mathrm{L}]^2$	λ^2
Volume	$[\mathrm{L}]^3$	λ^3
Density	$[M][\mathrm{L}]^{-3}$	1
Mass	[M]	λ^3
Time	[T]	$\lambda^{0.5}$
Frequency	$[\mathrm{T}]^{-1}$	$\lambda^{-0.5}$
Velocity	$[\mathrm{L}][\mathrm{T}]^{-1}$	$\lambda^{0.5}$
Acceleration	$[\mathrm{L}][\mathrm{T}]^{-2}$	1
Force	$[M][\mathrm{L}][\mathrm{T}]^{-2}$	λ^3
Moment	$[M][L]^2[\mathrm{T}]^{-2}$	λ^4
Power	$[M][L]^2[\mathrm{T}]^{-3}$	$\lambda^{3.5}$
Stress	$[M][L]^{-1}[\mathrm{T}]^{-2}$	λ
Mass moment of inertia	$[M][\mathrm{L}]^2$	λ^5
Area moment of inertia	$[\mathrm{L}]^4$	λ^4

The Froude similarity was employed instead of the Reynolds similarity since the waves' effect on the dynamics is significant in this study. The scale effects on the measured values should be minimized, hence the scaling ratio should be as large as possible.

Therefore, the weight, power, and thrust force values will be greater and consequently easier to measure. A larger model turbine cannot be built in the wave flume; thus, a scale ratio that is just large enough to fit inside the wave flume must be chosen. Therefore, the model scale is chosen as 1/40.

3.3.2. Wave Channel and Wave Generator

Experiments were conducted in a 40-m-long, 1-m-wide, and 1.4-m-deep wave channel in the IYTE Civil Engineering Department's hydraulic laboratory. As shown in Figure 3.6, a dissipation beach composed of rocks of varying sizes and a gradient of 1/5 is placed at the opposite end to absorb waves that would otherwise reflect backward.

Furthermore, the waves travel to the back of the piston, causing splashes and increasing the risk of motor damage due to the interference between the generated and reflected waves. To dampen the waves in this location, a steel cage filled with absorbent material (plastic sponge) was installed (Figure 3.6).

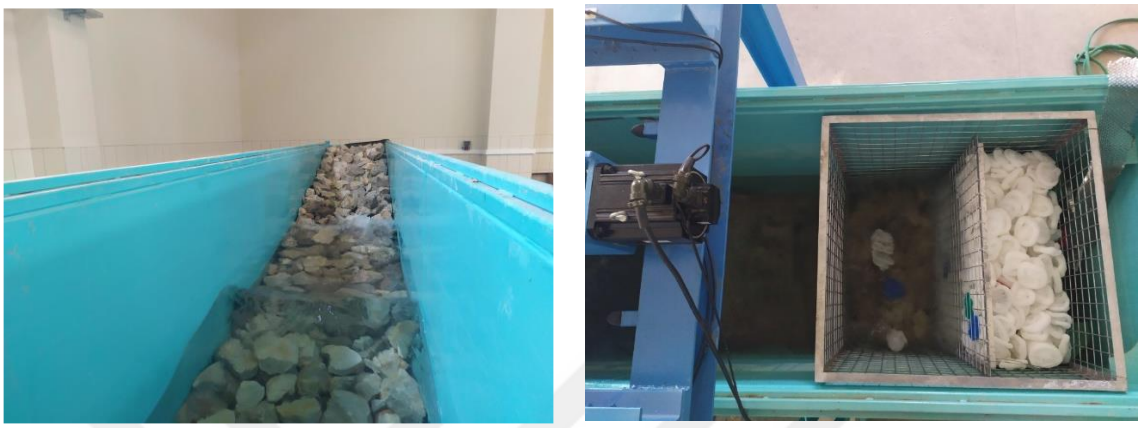

Figure 3.6: Dissipation beach (left) and Absorbent steel cage (right) (Source: Aktaş, 2020)

For regular and irregular wave studies in the channel, a piston-type wave generator with a 5-kW servo motor, a stroke length of 1 m, and a maximum speed of 0.83 m/s was designed and built (Aktaş, 2020). To produce a regular wave, the desired time series must be converted into piston motion. Therefore, first, the time series according to the regular wave profile was obtained, and in accordance with the first-order linear theory, Hughes (1993) and Dean and Dalrymple (1984) gave the following Eq. (3.30) and (3.31), the piston movement to create the regular wave profile was calculated.

$$x_0(t) = \frac{S_O}{2} . \sin\sigma t \tag{3.30}$$

$$\frac{H}{S_0} = \frac{4\sin h^2 kh}{\sin 2kh + 2kh} \tag{3.31}$$

here; h is the water depth, S_0 the required piston stroke and the H wave height.

A code has been written using MATLAB to generate irregular waves. Inputs include wave height, period, spectrum properties, and depth of water. Obtaining a

frequency spectrum with the required wave properties is the initial phase of this code (conforming to the information entered by the user). After the spectrum was obtained, an irregular wave time series was generated. The amplitude and phase angle of the wave are required for this. The wave time series was constructed by combining the wave amplitudes acquired from the wave spectrum with random phase angles using DSA, also known as the "deterministic spectral amplitude" approach (Özbahçeci, 2004). To produce the irregular wave, it is necessary to convert the desired time series into piston motion. The following relationship between the spectrum of irregular waves and the spectrum of piston motion is employed.

$$S_{\eta\eta}(\omega) = (m_{1n})^2 S_{wb}(w_n) \tag{3.32}$$

$$m_1 = \frac{4\sinh(kh)}{\sinh(2kh) + 2kh}[\sin(kh) + (1 - \frac{\cos(kh)}{k(h+l)}] \tag{3.33}$$

here; S refers to the component of the wave spectrum, S_{wb} refers to the component of the piston movement spectrum and m_{1n} is the transfer function.

A MATLAB GUI has been used to construct a user-friendly interface where wave parameters, water depth, and experiment duration can be entered to generate waves for use in experiments. Therefore, for wave generation, the user should first choose between regular and irregular waves. For the regular wave, wave period, wave height, time step, and duration parameters should have been entered in the interface, then the wave and piston time series were generated initially. Figure 3.7 depicts, in the upper graph, the regular wave time series, and, in the lower graph, the second-order solution of the piston motion. The produced piston time series are then communicated with Simulink, and the required signals are sent to the wave generator's motor.

For the irregular wave, three spectrum alternatives are available: Pierson-Moskowitz, JONSWAP, and Bretschneider-Mitsusu. The irregular wave tab was constructed in a similar scheme: the data number N, the time step dt, the water depth d, the apparent wave height Hs, the peak period T_p, and the spectrum type were identified. By modifying the seed value in the interface, an infinite number of irregular waves with the same wave characteristics can be created. After identifying the wave characteristics,

the relevant figures are displayed on the screen so that the necessary adjustments may be made, and the data to be processed by Simulink is sent in the background. Figure 3.7 depicts an example of a time series and spectrum of irregular waves.

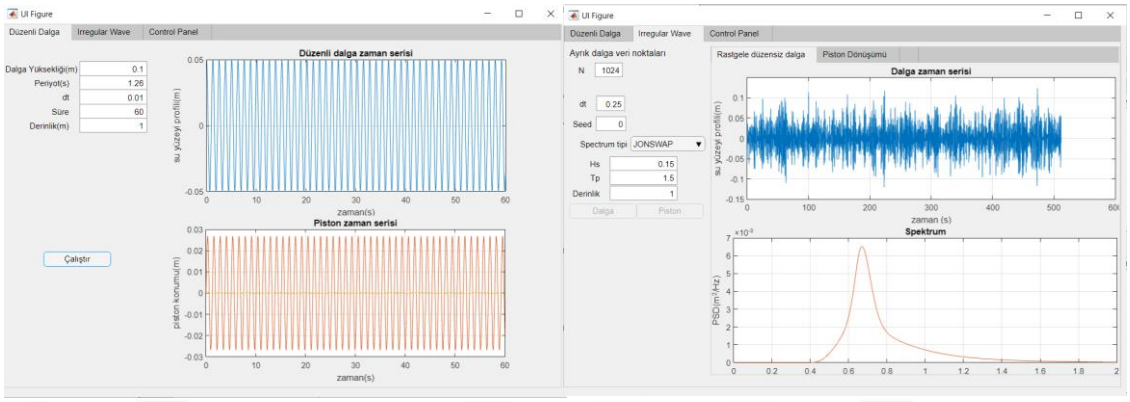

Figure 3.7: Regular wave GUI (left) and Irregular wave GUI (right) (Source: Özkol et al., 2022)

After installing the wave gauges, regular and irregular waves with varying wave heights and times were generated, and measurements were taken. Figure 3.15 compares the targeted and measured wave heights and periods that are produced in the channel. Additionally, the y=x line is drawn to illustrate the relationship between the target and the measurement. According to Figure 3.8, results for regular waves were very similar to the target. Even though the measurement results for irregular waves are fairly similar to the predetermined targets, it is evident that there are minor deviations. This difference was determined to be under 10%.

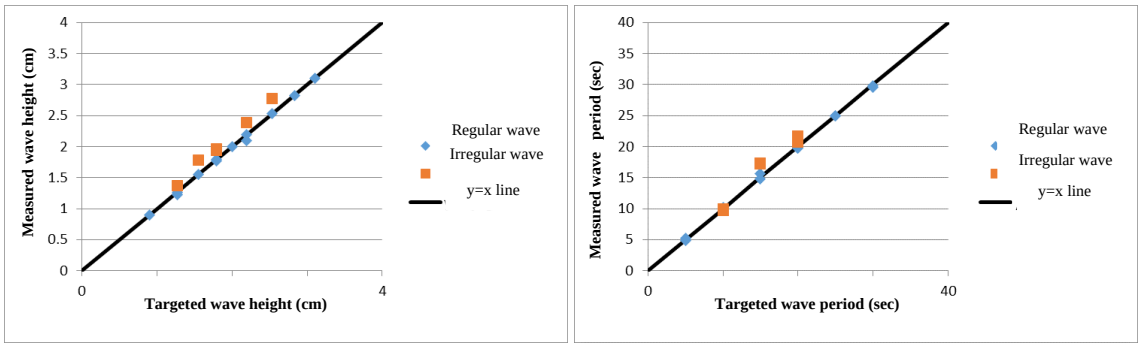

Figure 3.8: Comparison of targeted and channel generated wave heights (Source: Özkol et al., 2022)

To confirm that the irregular waves were generated as anticipated, their spectrum and wave height distribution were also examined. Although waves observed in nature appear irregular and random, studies have revealed that wave heights conform to a distribution. This distribution is the Rayleigh distribution. The total distribution function, according to the Rayleigh distribution, is provided below.

$$P(H < H') = 1 - \exp(-\alpha^2 x^2) \quad where\ x = H'/H^*$$

$$\alpha = \begin{cases} \frac{\sqrt{\pi}}{2} : if\ H^* = H_{ort} \\ \sqrt{\pi} : if\ H^* = H_{1/3} \end{cases} \tag{3.34}$$

It was verified whether the irregular waves created in the channel by the wave generator fit the Rayleigh distribution. The data points should be close to the y=x line if the waves are Rayleigh-fitted.

Figure 3.9 depicts that the created irregular waves fit the Rayleigh distribution as intended.

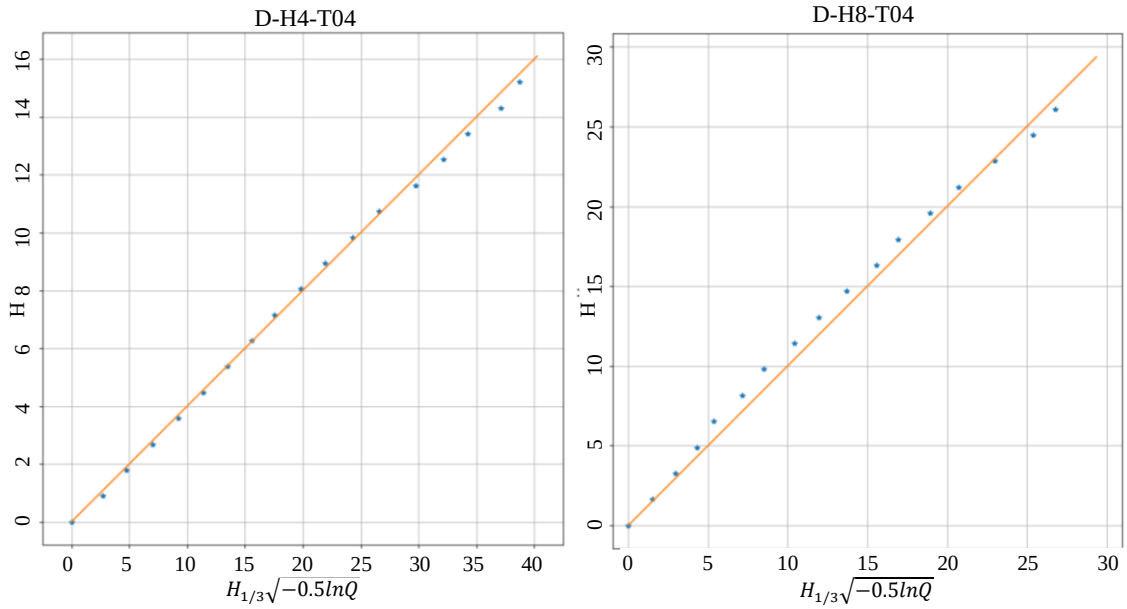

Figure 3.9: Conformity of Rayleigh distribution in different irregular wave cases (Source: Özkol et al., 2022)

3.3.3. Wind Nozzle

Due to the Froude similarity applied at a ratio of 1/40, the speed ratio must be around 6.5. The wind speeds were estimated to be between 15 and 25 m/s, as the focus of this investigation was on the condition of the turbines in extreme conditions. Consequently, the wind speeds on this wave channel range between 2.3-3.80 m/s according to the Froude scale. Utilizing a narrowing nozzle to reduce turbulence and achieve uniform velocity distribution is commonly practiced in wind tunnel applications. When this contraction percentage is compared to other examples, it has been observed that shrinkage percentages greater than 1/5 produce favorable outcomes (Mehta and Bradshaw, 1979). Moreover, in the contraction parts of small wind tunnels, it has been seen that polynomials of the fifth or fourth order provide successful performance. In consideration of the ease of manufacture, the nozzle was designed using polynomials of the fourth order for this purpose (Erol,2020). Then, two different narrowing rates of 1/2 and 1/4 were chosen, and two air ducts, considering the width of the wave channel (1 m) depicted in Figure 3.10, were built for use in different experiments.

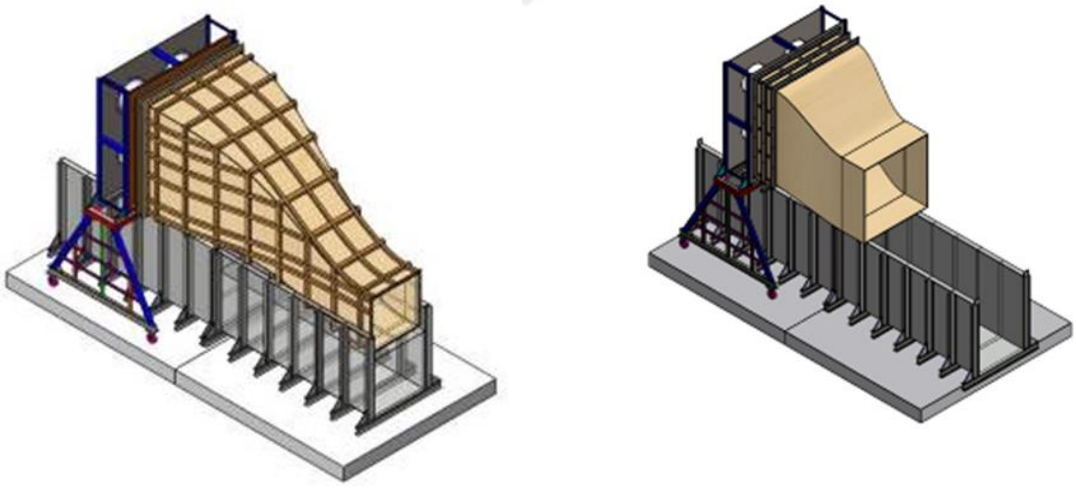

Figure 3.10: Air channels designed for the study (Source: Arıdıcı, 2022)

In addition, a perforated plate in the first portion and a honeycomb in the second section are placed at the entry to evenly distribute and direct the flow throughout the cross-section of the wind nozzle. The perforated plate has a 1 mm thickness, 9 mm diameter holes, and a 12 mm distance between hole centers. Honeycomb is 15 mm thick,

features 10 mm cells, and has 0.2 mm thick walls. Also, to provide a gradient and homogeneous wind profile, the wind nozzle's entrance is equipped with four fans whose speeds may be separately controlled.

3.3.4. Wind Turbine Model

Due to the wave channel's dimensions of 40 m in length, 1 m in width, and 1.4 m in depth, it was not possible to model a 5 MW wind turbine, so it was decided to continue the research using a model designed for a 300-kW wind turbine. The Northel POYRA P36/300 wind turbine is chosen for the turbine model. The design of the model turbine assumes that the tower and the blades behave as stiff, inflexible bodies. Using the 1/40 scaling factor and the thrust force of the turbine operating at 20 m/s, the blade and rotor design parameters for the model are determined (Erol, 2020). The desired rotor model specifications are shown in Table 3.4.

Table 3.4: Model rotor specifications

Parameters	Reference	Scaling Factor	Model
Hub diameter	2 m	λ	0.05 m
Rotor diameter	36 m	λ	0.9 m
Wind speed	20 m/s	$\lambda^{0.5}$	3.16 m/s
Rotor speed	50 rpm	$\lambda^{-0.5}$	316.22 rpm
Power	320 kW	$\lambda^{3.5}$	0.79 W
Power coefficient	0.064	1	0.064
Thrust	18.9 kN	λ^{3}	0.296 N
Thrust coefficient	0.076	1	0.076
Blade mass	1774 kg	λ^{3}	27.72 g

During the airfoil selection phase, the AG04 (Martin, 2011), SD7032 (Bayati, 2017), and Ishii airfoil (Anyoji et al., 2014) designs were examined, and performance tests were conducted. Under the parameters of 3.16 m/s wind speed, 316.22 rpm, and 4.71 TSR, modeling calculations were conducted using three different blades, each produced by one of these three airfoils. Ishii is selected after these tests because of its favorable power behavior (Figure 3.11). Due to its complex geometry, which consists of thin sections and twisted surfaces, the model airfoil is the most difficult component to manufacture in this design. In certain locations, the thickness of the blade is less than 1

mm, requiring the fabrication of a hollow blade with an extremely thin shell. Consequently, these blades are manufactured by 3D printing (Figure 3.12)

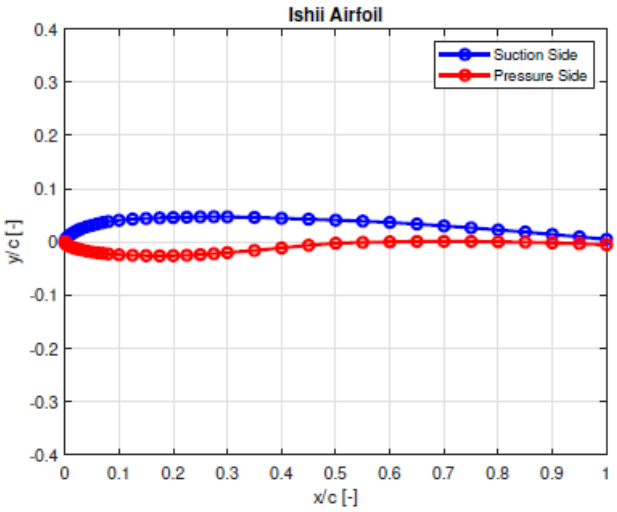

Figure 3.11: Ishii airfoil section (Source: Arıdıcı, 2022)

Figure 3.12: STH printed blade (Source: Erol, 2020)

Based on the scaling approach, it is essential to estimate the tip speed ratio to get as close as possible to satisfying dynamic similarity in the aerodynamic part. The BEMT study reveals that the model turbine cannot achieve 316.22 rpm at 3.16 m/s wind speed; hence, an attached motor must drive the rotor to fulfill the needed tip speed ratio. Since a turbine tower will be installed on a floating platform, the loads on the rotor will vary as the platform moves, but the motor should continue to rotate at the same speed regardless of the loads. It is essential to get a strong engine and a driver that can manage these conditions. The motor and driver that can be utilized with PID assistance were thus deemed suitable for this investigation. Due to the importance of the motor's weight, the 98 g motor stated in the table is the best option.

3.3.5. Modified Version of Innovative Floating Platform for 300 kW Wind Turbine

Since the new floating platform was developed for a 5 MW reference wind turbine, it was first redesigned to accommodate a 300-kW wind turbine. Then, the water depth was chosen as 40 m to validate the model designed for the 300-kW turbine, and all numerical analyses performed on the 5 MW model were repeated; as a result, it was determined that the performance and characteristics were similar to those of the 5 MW model. The model designed for a 300-kW turbine is shown in Figure 3.13.

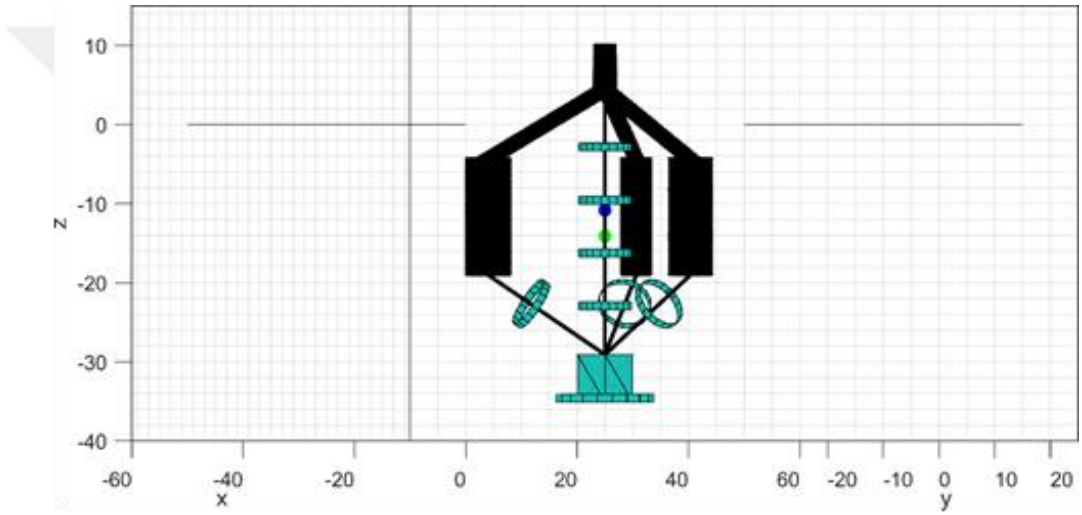

Figure 3.13: Novel platform design for 300 kW wind turbine and 40-m water depth (Source: Özkol et al., 2022)

3.3.6. Manufacture of Innovative Floating Platform for Experimental Studies

Using the Froude scale, the model of the new platform with a scale ratio of 1/40 was designed to be used in experiments. In this model, the floaters, which will be constructed from concrete in the prototype, are manufactured from plastic pipes. Likewise, PVC pipe was used in the laboratory model to represent the steel pipes used in the prototype as arms of floaters.

Figure 3.14 shows the innovative platform model and the technical drawing. Table 3.5 lists the properties of the novel platform model to be investigated.

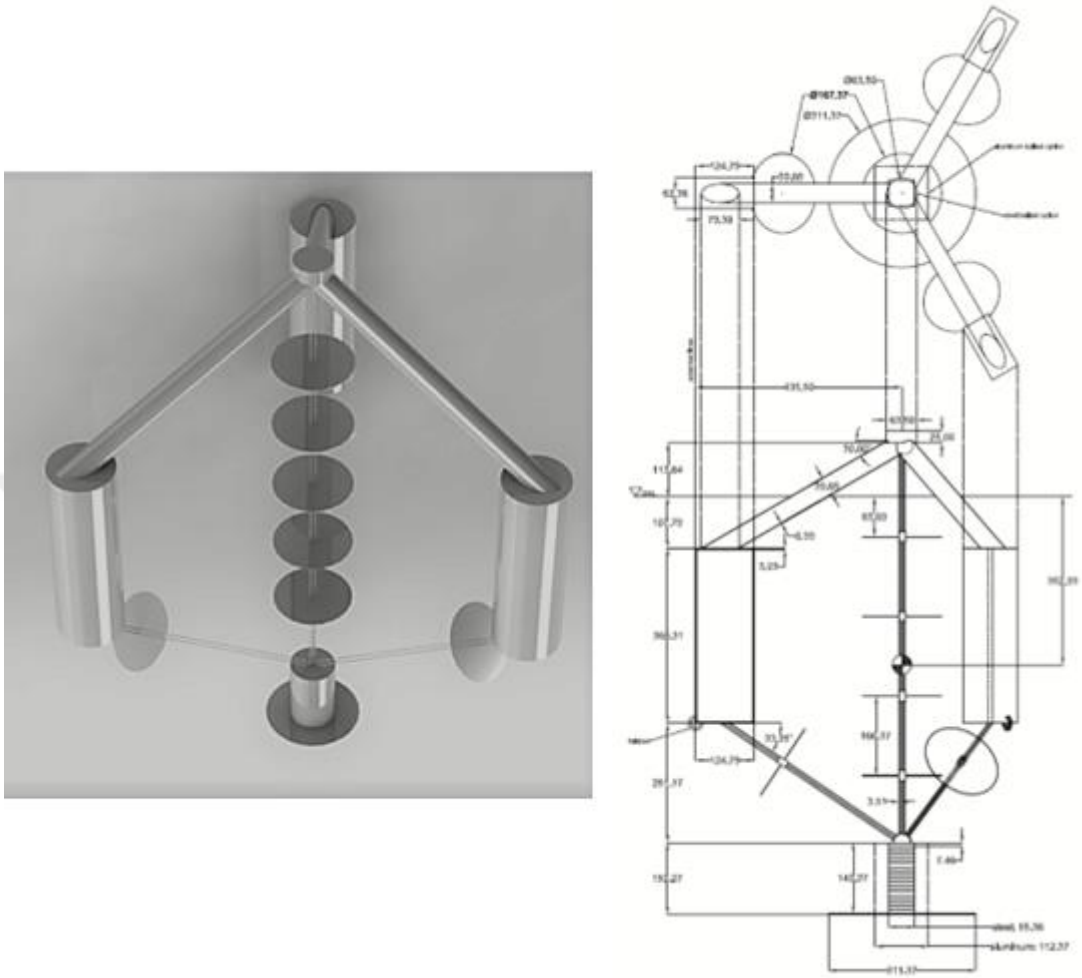

Figure 3.14: The appearance of the innovative platform model(left) and the technical drawing created for manufacturing(right) (Source: Özkol et al., 2022)

Table 3.5: Novel platform properties of lab scale model

Overall System Properties	
Total Draft (mm)	876.54
Freeboard (mm)	113.64
Mass (total system) (g)	9203.45
CG below SWL (total system) (mm)	352.93

(cont. on next page)

(table cont.)

Platform Topology		
Buoyant floaters		
Number of buoyant floaters/legs	3	
Angle of buoyant legs in the vertical plane (deg)	30.00	
Outermost radius of the platform (mm)	435.50	
Depth to top of buoyant floaters below SWL (mm)	107.79	
Depth to bottom of buoyant floaters below SWL (mm)	476.10	
Width of buoyant floater (mm)	62.38	
Length of Buoyant floater (mm)	124.75	
Wall thickness of buoyant floater (mm)	3.03	
Diameter of buoyant legs (mm)	39.65	
Wall thickness of Buoyant leg (mm)	0.99	
Ballast		
Ballast mass in air (g)	PVC: 4885.15	Steel: 3662.06
Ballast mass in water (g)	3204.30	
Ballast CG below SWL (mm)	801.91	
Ballast height (mm)	149.27	
Ballast width (mm)	PVC: 110	Steel: 55.38
Chain bundles		
Number of middle chain bundles	4	
Nominal diameter of middle chains (mm)	~2.00	
Number of chains in the bundle	2	
Bundle air mass per unit length (g/m)	159.20	
Length of vertical bundle (mm)	840.91	
Length of side bundle (mm)	465.71	

(cont. on next page)

(table cont.)

Heave plates	
Number of vertically suspended heave plates	4
Number of side suspended heave plates	3
Number of ballast heave plates	1
Diameter of suspended heave plate (mm)	167.37
Diameter of ballast heave plate (mm)	311.37
Thickness of heave plates (mm)	1.00
Mass of a suspended heave plate in air (g)	175.62
Mass of a ballast heave plate in air (g)	607.77

3.3.7. Measurement System

3.3.7.1. Wave Gauge

To measure the wave profiles created in the channel, 60 cm-long resistance-type wave gauges manufactured by the Wallingford Company in England were utilized in our laboratory. Wave gauges were installed inside the wave channel, calibrated, and tested. Figure 3.15 depicts the location of wave meters inside a canal. The wave gauges deliver the voltage created by the change in water level analogously to the data logger, which subsequently converts the analog signal into a digital signal. The voltage obtained during the calibration procedure is converted to the water level using a custom-written algorithm.

Figure 3.15: Wave gauges installation in the wave channel (Source: Özkol et al., 2022)

3.3.7.2. Load Cell

During the physical model experiments, load cells were used to measure the chain tensions of the floating platform to confirm that the desired chain prestresses were achieved at the beginning of the experiment and to examine the tension behavior of the chains under various wave and wind conditions. Scaled chain pretension values were determined to be 0.87N, which is equivalent to 89.23 grams of force. To measure chain tension, load cells with a 10 V output range and a capacity of 0-5 kg were utilized. The load cells are connected to the DAQ, which provides communication with the piston wave generator, and the Simulink model stores the measured data. The data are then processed in MATLAB. The load cells have an IP67 protection class, which means they are resistant to dust and short-term water contact. During physical experiments, however, load cells whose chains will be submerged in water must be able to function continuously underwater. In order to make load cells water-resistant, they are dipped in white mastic silicone and left to dry (Figure 3.16).

Figure 3.16: Load cell (Source: Özkol et al., 2022)

To calibrate the load cells, the voltage value read when the load cells are attached to the fairlead was set to zero, then known weight and volume loads were loaded under water and the voltage values read in Simulink were recorded. Since the loads are weighed underwater, the buoyancy forces acting on them are eliminated, and after mass corrections, a linear relationship was found between the loads and the measured voltage values (load = a*voltage + b). In future trials, the acquired conversion functions were employed to transform the read voltage values into gram-force values.

3.3.7.3. Image processing tool

Using an image processing approach, the movement of the floating wind turbine model under wave and wind conditions was examined over time. During the studies, colored table tennis balls are positioned on the turbine pole, and images are captured at a rate of 120 Hz using a high-resolution camera (GoPro). The processing of the recorded videos is achieved using the open-source application Tracker. This software identifies video frames to be displayed sequentially. For instance, a 60-second video captured with a 120 Hz camera has 7200 frames (120 x 60). After running the Video Tracker application, the first frame of the video is recognized as the reference frame, and an origin point is chosen from the program settings in this frame. The actual distance between the balls is 0.725 meters, which is the length of the calibration line traced from the top ball to the bottom ball. The application self-calibrates by comparing the length of the calibration line in pixels to the length specified in meters. The computer then records the horizontal and vertical distances to the origin point based on time by tracking these balls in each frame of the movie. Figure 3.17 illustrates the image processing software.

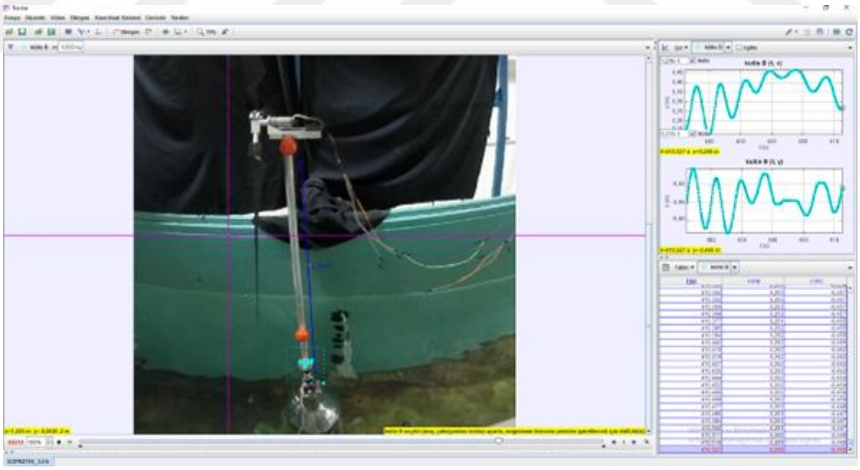

Figure 3.17: Image processing software (Source: Özkol et al., 2022)

Here, the junction of the purple and blue lines represents the origin, while the purple line represents the calibration line. The graph of the tracked ball's location in the horizontal and vertical planes as a function of time is shown in the upper right window, while the same numbers are displayed in a table in the bottom right window. Finally, using MATLAB code, the processed position data were divided into the surge, heave, and pitch motions.

3.3.7.4. Strain gauge

The measurement of the thrust on the turbine tower cannot be acquired directly; rather, the total dynamic force on the tower was calculated by measuring the strain at the base of the tower using a strain gauge.

In this work, a BF350-3AA/1.5AA strain gauge module with one gauge and one amplifier was used. This module outputs an analog voltage between 0 and 3.5 V. As illustrated in Figure 3.18, the gauges are mounted at a 90° angle on the tower.

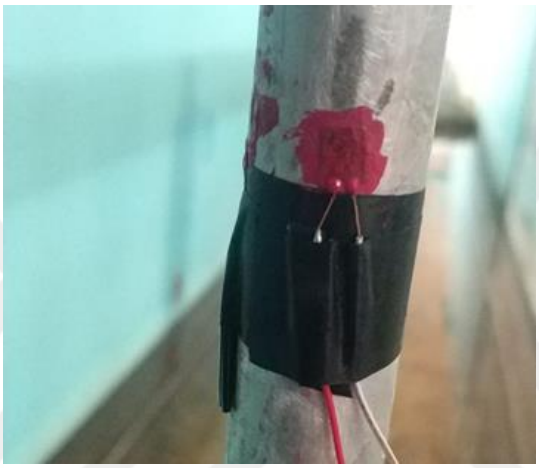

Figure 3.18: Strain gauge sensor at the base of the tower (Source: Özkol et al., 2022)

The strain gauges were first attached to the Wheatstone-bridge and the amplifier to measure the resistance change. At 100 Hz, the amplifier's output signals were delivered straight to the computer through a 16-bit data acquisition card (PCI1710HGU) and recorded.

Since the strain gauge's resistance change is translated to the voltage by the Wheatstone-bridge, the device must be calibrated to determine the force causing the voltage change. By applying known forces to the tower and measuring the voltage values that resulted, the calibration measurement was performed, and it was successful.

3.3.7.5. Hot-Wire

A hot-wire anemometer was used to measure the velocity of the flow exiting the wind nozzle and the changes in flow velocity that will occur around the model wind turbine. The hot-wire system operates on the principle of heat transfer between the heated wire and the surrounding cold airflow. This principle establishes a relationship between fluid velocity and electric voltage. The primary function of the electronic circuit of the hot-wire is to deliver a regulated quantity of electric current to the wire portion. The calibrated constant-temperature hot-wire anemometer produces a variable current based on fluid velocity to maintain constant wire temperature (Bruun, 2009). First, in order to use the hot wire anemometer method, it is necessary to calibrate the hot wire sensor with a prepared calibration mechanism. For this, a wind nozzle was manufactured to provide the laminar flow (Figure 3.19), and the turbulence was reduced by adding metal grids to the nozzle.

Figure 3.19: Jet flow nozzle for experiments (Source: Arıdıcı, 2022)

The wind speed given to the anemometer was measured with a High Wycombe L-type pitot tube connected to the Dwyer Model M1430 Microtector U-manometer. The h value in the Dwyer manometer, which shows the pressure difference between the two outlets of the pitot tube, was taken many times for the same condition, and the Bernoulli equation was used to determine the wind speed at the exit of the nozzle. The wind speed at the outlet was calculated. For hot-wire calibration, the IFA300 constant temperature anemometer system was used. After the necessary connection settings and presets were

made, the bridge voltage value was recorded by giving 20 different speed values between 0-5 m/s. Figure 3.20 depicts a calibration curve with a high level of agreement between the voltage value that varies with wind speed and the recorded manometer data, as determined by a fourth-order polynomial fit.

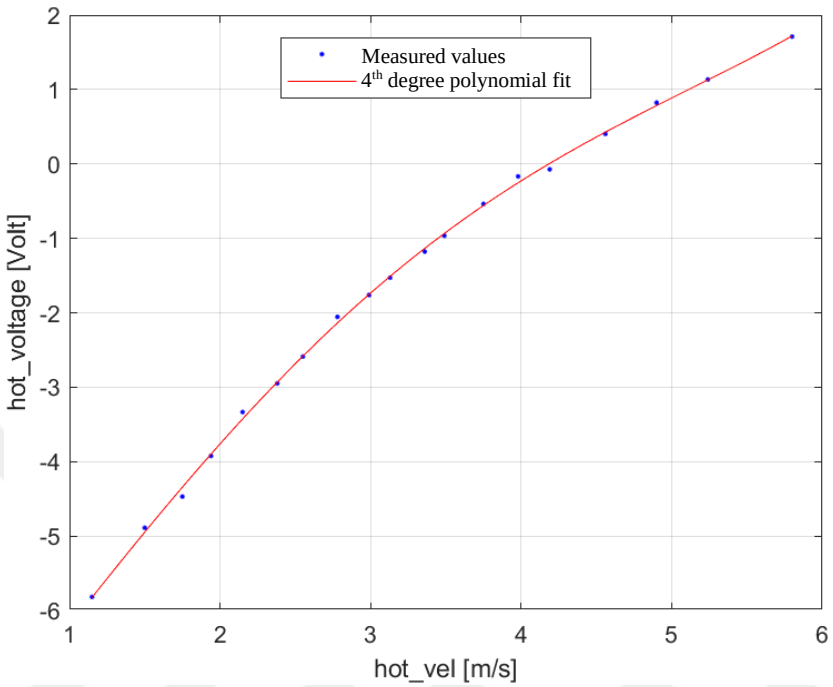

Figure 3.20: Hot wire calibation graph (Source: Arıdıcı, 2022)

CHAPTER 4

EXPERIMENTAL RESULTS

Experimental studies were conducted in a 40m x 1m x 1.4m wave channel in the hydromechanics laboratory at IZTECH. In the studies, it was intended to examine the platform under a variety of wave conditions, ranging from mild to extreme. Therefore, wave heights ranging from 2 m to 12 m were applied to the model. Using the wave steepness formula, the periods corresponding to the wave heights were determined. The wave steepness formula is given in Eq. 4.1.

$$s = H/(\frac{gT^2}{\pi}) \tag{4.1}$$

In monochromatic waves, wave steepness is defined as the ratio of wave height to wavelength. The research implemented two different wave steepnesses, 0.02 and 0.04. While 0.04 enabled the examination of more recurrent wave periods, 0.02 enabled the examination of longer wave periods. The experimental wave parameters and value ranges are presented in Table 4.1.

Table 4.1: Experimental wave parameters and prototype value ranges used in the tests

Parameter	Range
Wave Height	2-12m
Wave Steepness	0.02, 0.04
Wave Period	5.69s-19.6s

In the experimental study, free decay tests, quasi-static tests, regular wave tests, and irregular wave tests were conducted. While tests with only wind was performed, regular and irregular wave experiments were repeated together with the wind, produced by the fans through the wind nozzle. The water depth was set to 1 m, and wave gauges and load cells were calibrated each experiment day. The surge, heave, and pitch responses of the platform were obtained by applying image tracking techniques to the videos captured with the camera during the test. Also, the load cells simultaneously measured tensions occurring in all three cables.

4.1. Free Decay Tests

Firstly, free decay tests (FDT) were conducted in three degrees of freedom, namely surge, heave, and pitch, to determine the natural period and damping behavior of the structure. Experimental data were used to determine the numerical model's added mass and damping coefficients. During surge decay testing, an external force is applied to displace the floating platform from its equilibrium position in the positive X direction. When the water in the channel stagnates, the force is released, and the platform begins to oscillate until it reaches equilibrium. For the heave decay test, the platform is displaced in the negative Z direction, whereas for the pitch decay test, a torque is applied to force the platform to rotate about the positive y-axis. The platform is then allowed to oscillate until it reaches equilibrium again, similar to the surge movement.

As shown in Table 4.2, the free decay tests were done three times for every three degrees of freedom. Table 4.2 displays the duration in seconds, the first position in centimeters, and the first rotation in degrees. Also, the outputs of the free decay test are displayed in Figure 4.1.

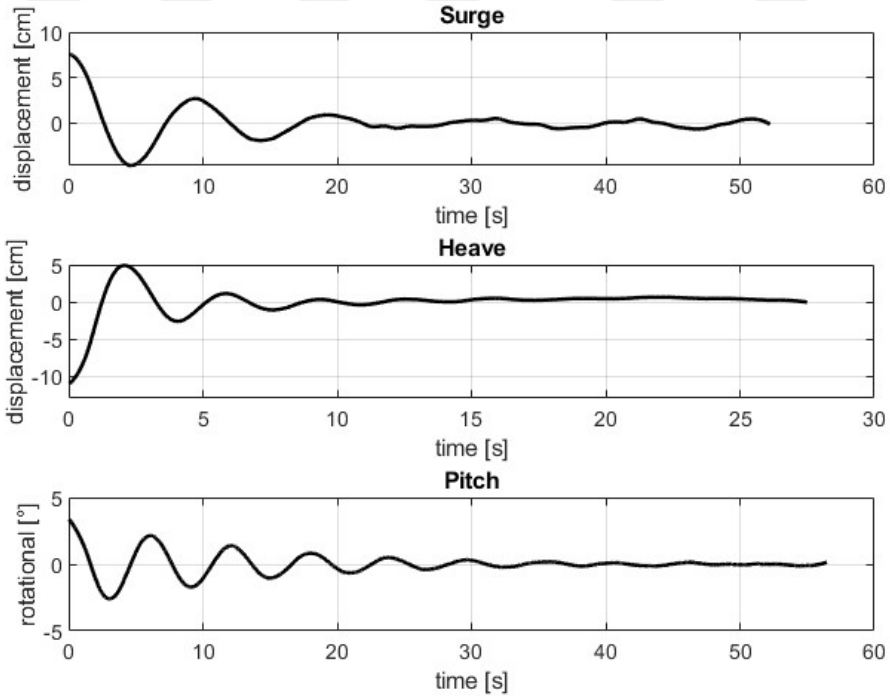

Figure 4.1: Free decay test result

Table 4.2: FDT duration and initial values of experimental model

	Surge		Heave		Pitch	
	Duration	Initial Location	Duration	Initial Location	Duration	Initial Rotation
SET1	52	7.58	27	-11.00	56	3.35
SET2	66	14.00	26	-9.70	58	6.03
SET3	53	16.40	54	-14.35	71	10.88

The wave period, which is the time between two wave crests or troughs, was determined for each test and is shown in Table 4.3.

Table 4.3: Natural period of innovative platform for each 3 DoF

	Surge Period [s]	Heave Period [s]	Pitch Period [s]
SET1	9.7	3.6	6
SET2	10.2	3.8	6.2
SET3	10.5	3.7	6.1

4.2. Quasi-Static Tests

In addition to the free decay tests, the behavior of the chains was examined by measuring the chain tensions by applying the longitudinal displacement to the model in still water. Figure 4.2 depicts the tensile forces in the anterior chain (chain 1), whereas Figure 4.3 displays the tensile forces in the posterior chains (chains 2 and 3).

As expected, the chain in the direction of the displacement loosens, but the chain on the other side stretches and attempts to return the platform to its initial position. Load cells positioned between the platform fairlead and the mooring chains were used for measurements.

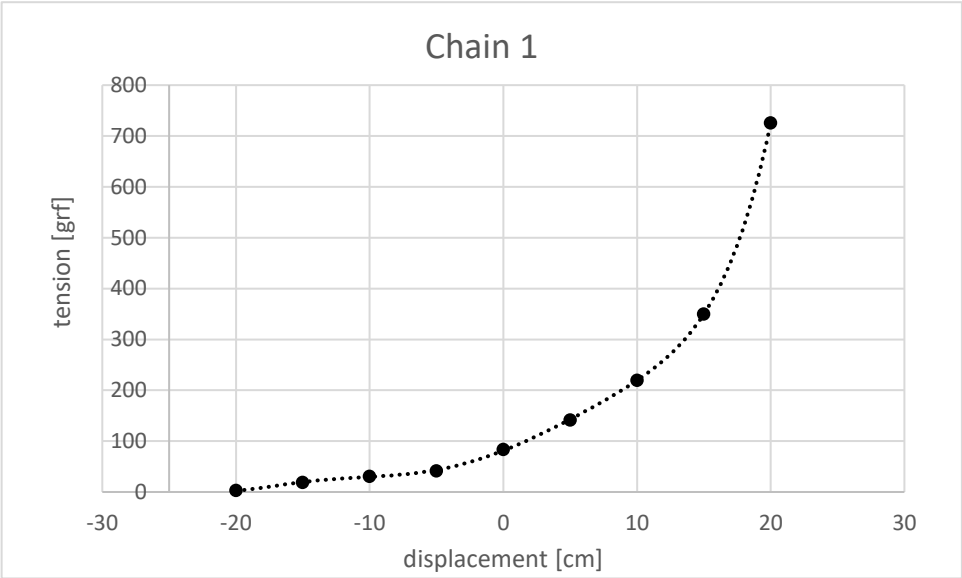

Figure 4.2: Quasi-static test response of chain 1

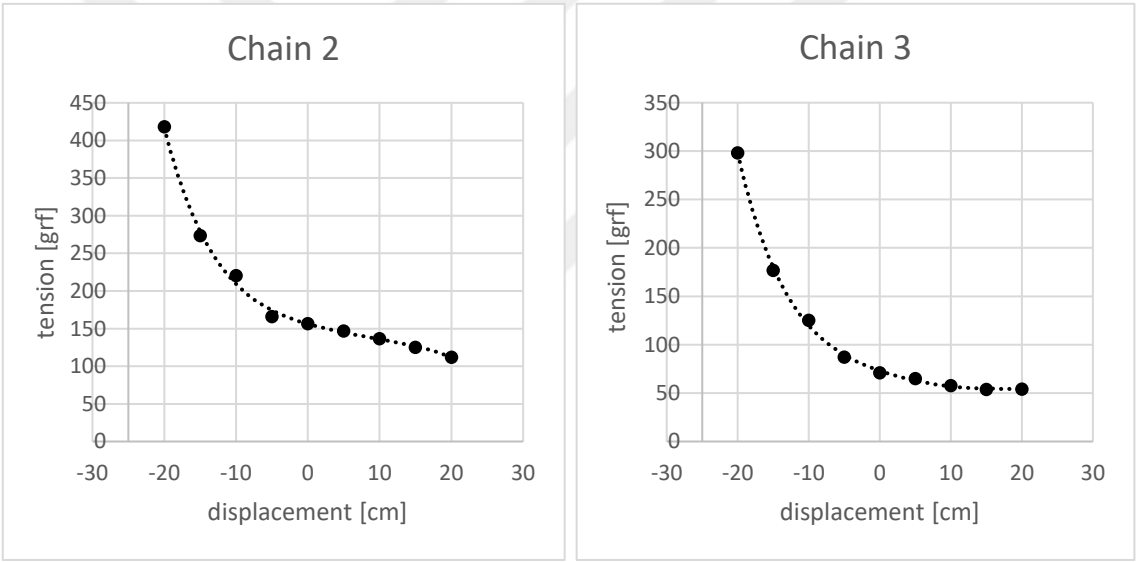

Figure 4.3: Quasi-static test response of chain 2&chain 3

4.3. Regular Wave Tests

Following the free decay and quasi-static experiments in still water, 12 tests with regular waves were conducted. Regular waves are waves with a constant wave height and wave period that are extremely rare to occur in nature. However, it is beneficial for observing the structure's response in the physical and numerical model tests under specific wave periods and wave heights. Table 4.4 lists the regular wave tests and parameters used in the experiments. The name of the tests was determined by the prototype wave height

and wave steepness. For instance, if the wave height is 8 m and the wave steepness is 0.04, the wave is represented as D-H8-T04.

Table 4.4: Regular wave tests and parameters used in the experimental study

Test Label	Wave Height [cm]	Wave Period [s]
H2T02	5.49	1.27
H4T02	10.87	1.79
H6T02	16.17	2.29
H8T02	20.02	2.53
H10T02	25.6	2.77
H12T02	32.06	3.1
H2T04	5.5	0.88
H4T04	10.66	1.26
H6T04	15.3	1.55
H8T04	20.06	1.74
H10T04	25.22	2
H12T04	29.53	2.18

In order to avoid wave reflection, the duration of the experiment was set at 60 seconds. As stated previously, the experiments were recorded with a camera for image processing. Likewise, chain tensions were recorded using load cells. Chain1(anterior) is in the direction of the wave generator and Chain2&3(posterior) are in the opposite direction. Surge, heave, and pitch time-based responses of the novel platform for the D-H8-T02 and D-8-T04 test conditions are shown in Figures 4.4 and 4.5, respectively.

In addition, Figures 4.6 and 4.7 illustrate the tensions in the anterior and posterior chains under D-H12-T02 and D-H12-T04 conditions in the time domain.

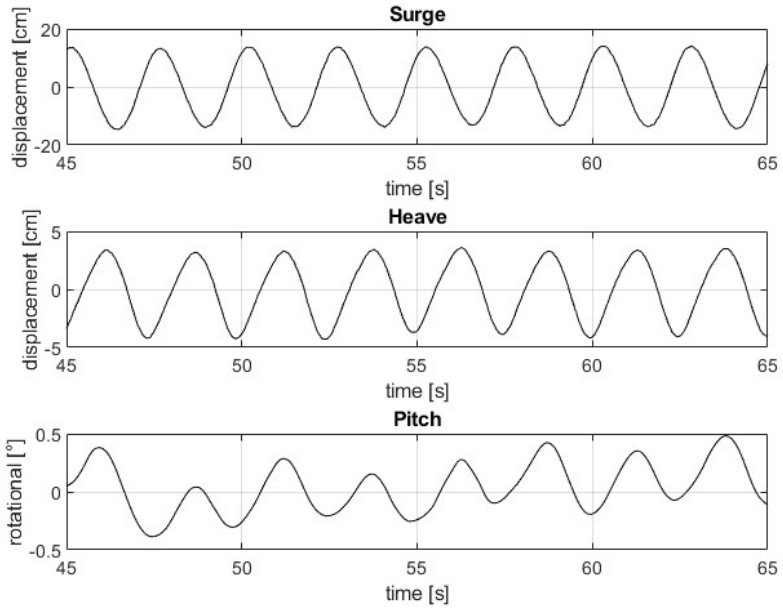

Figure 4.4: Surge, heave, and pitch responses of novel platform for the D-H8-T02 test as time series

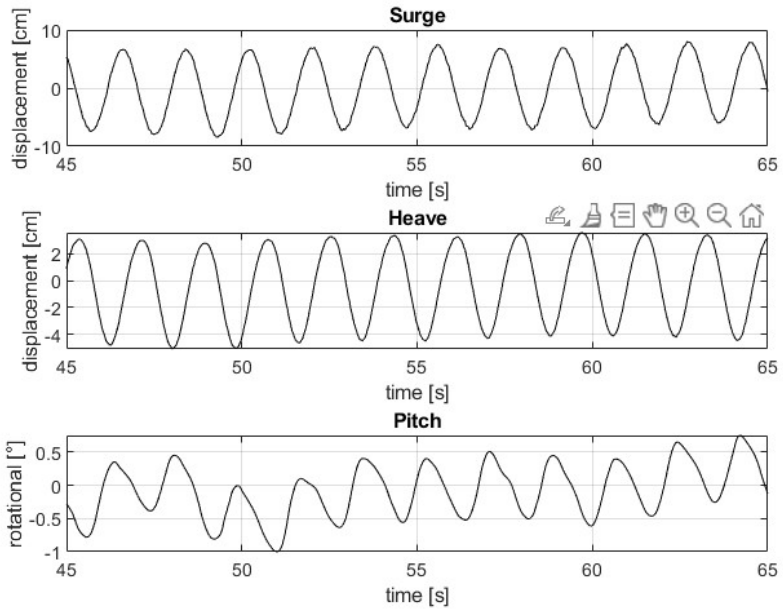

Figure 4.5: Surge, heave, and pitch responses of novel platform for the D-H10-T02 regular wave test as time series

As can be seen in Figures 4.4 and 4.5, the platform's rotational motion in the pitch direction, which is crucial for energy production, is low. As can be observed in Figures

4.4 and 4.5, the pitch response has a little irregularity. Those irregularities may be due to the image capture process, and since the pitch motion is small, the error effect on the pitch motion seems to be more apparent.

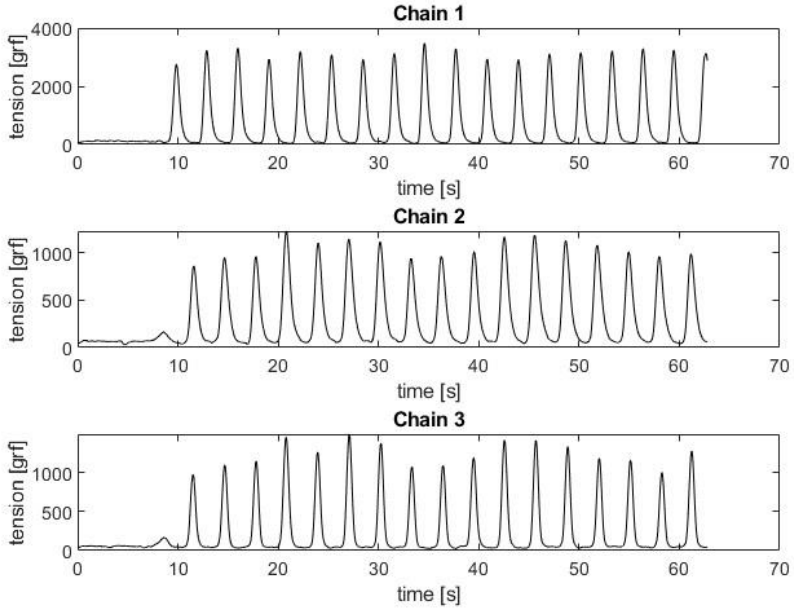

Figure 4.6: Chain tensions under D-H12-T02 regular wave test

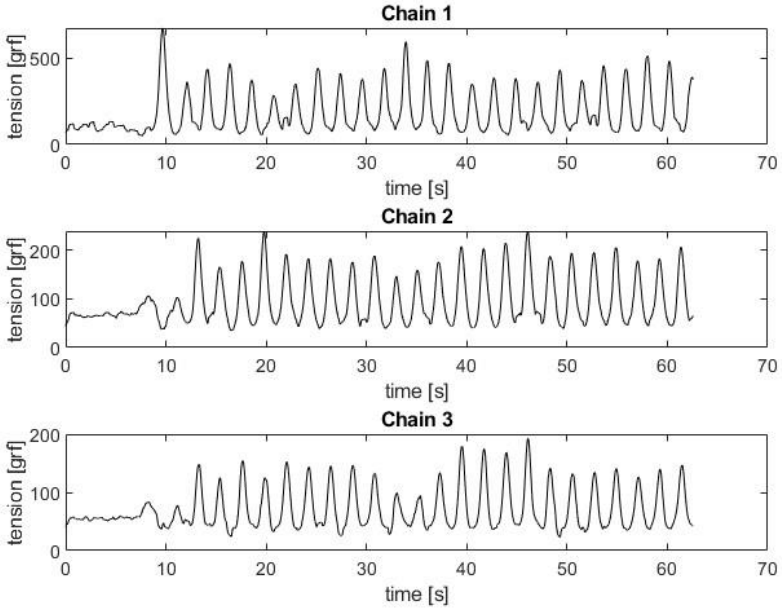

Figure 4.7: Chain tensions under D-H12-T04 regular wave test

Considering the chain tensions in Figures 4.6 and 4.7, it is obvious that Chain 1 has greater tension values than Chains 2 and 3. This can be explained by the fact that Chain 1 is positioned in the direction of the wave. The highest chain tensions measured for Chain 1, Chain 2, and Chain 3 illustrated in Figure 4.6 were 3483.5, 1224.8, and 1491.3 gr-force, respectively. In Figure 4.7, the highest chain tensions measured for Chains 1, 2, and 3 were 593.6, 239, and 192.9 g-forces, respectively.

4.4. Regular Wave and Wind Test

In this section, in addition to providing the structure with the regular waves indicated in Section 4.3, the wind was provided by activating the wind canal, and the propeller in the tower was activated by a motor. Then, experiments were conducted using both waves and the wind. Again, the motions of the floating system were recorded, and the surge, heave, and pitch responses were determined by image processing, while the tensions in the chains were recorded via load cells. Figures 4.8 and 4.9 depict the structural responses for the surge, heave, and pitch under experimental conditions D-H8-T02 and D-H8-T04, respectively. In Figures 4.10 and 4.11, the tensions measured in the chains under the extreme conditions D-H12-T02 and D-H12-T04 are presented, respectively.

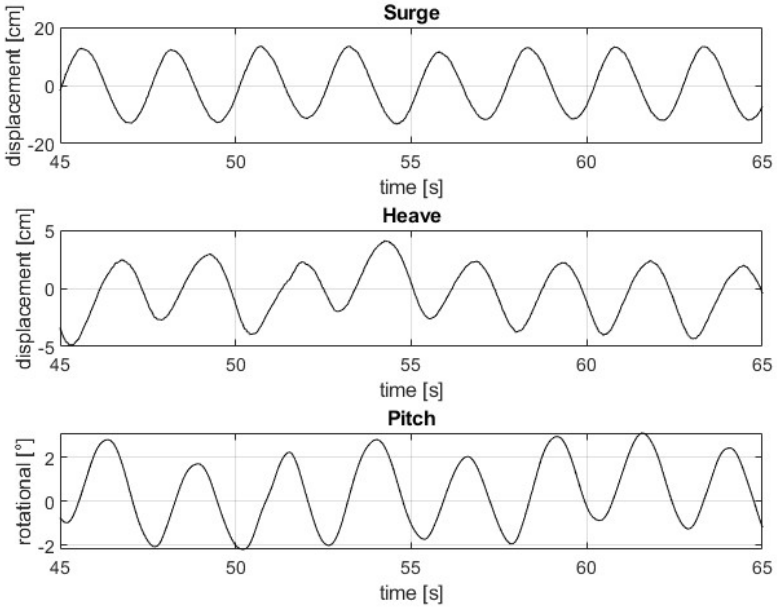

Figure 4.8: Responses of the novel platform under D-H8-T02 regular wave&wind test

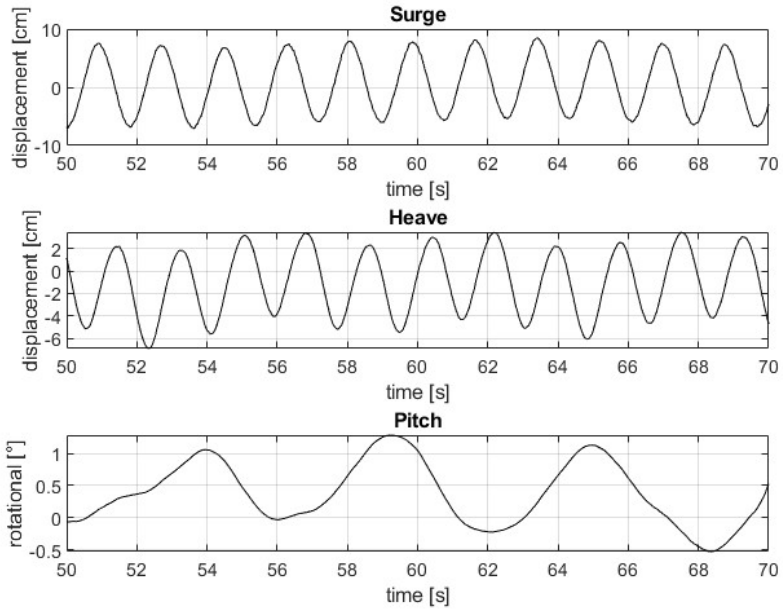

Figure 4.9: Responses of the novel platform under D-H8-T04 regular wave&wind test

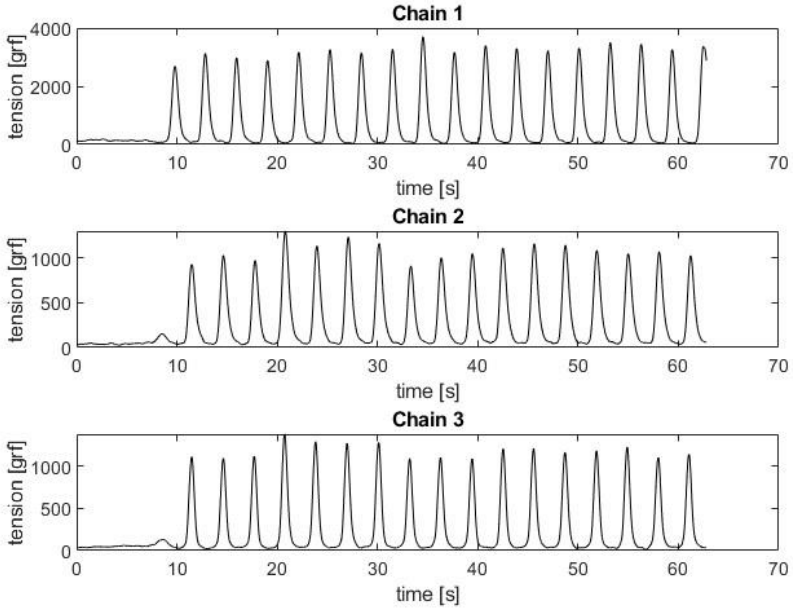

Figure 4.10: Chain tensions under D-H12-T02 regular wave&wind test

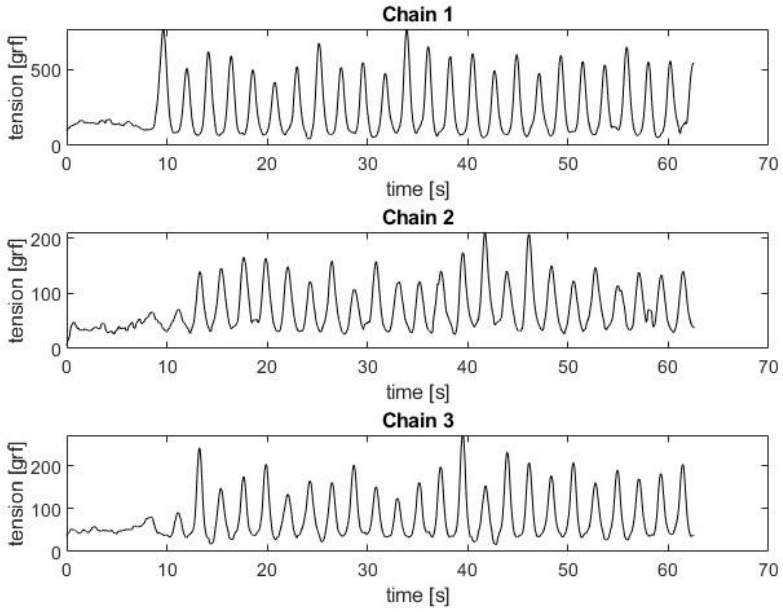

Figure 4.11: Chain tensions under D-H12-T04 regular wave&wind test

Analyzing Figures 4.8 and 4.9, it is evident that the pitch movement is minimal, whereas, in Figure 4.10, the highest chain tensions are 3708.4, 1297.3, and 1377.2 g-forces for Chains 1, 2, and 3, respectively; in Figure 4.11, the highest chain stresses are 766.9, 221.4, and 272.1 g-forces, respectively. As expected, Chain 1 has the highest tension.

4.5. Irregular Wave Test

Regular waves propagating at an unlimited range of frequencies and amplitudes create irregular waves, as is well known. In order to replicate the sea waves observed in nature, it is necessary to generate an irregular time series in the laboratory, characterized by varying wave heights and periods. With the aid of these irregular wave series, the behavior of the structure in natural seas is observed. In the irregular wave tests, at least 1000 waves were produced at each test. The data sampling interval was determined according to the wave period so that an individual wave could be recorded at a minimum of 10 discrete data points (Goda, 2010).

For instance, the test duration of an irregular wave series whose average period is defined as T_{mean} = 1s should be at least 1x1000 = 1000 s, and at least 10 surface profile

data should be measured by the wave gauges in 1 second, or the sampling frequency of the wavemeter should be at least 10 Hz. The number of data was chosen as 16384 in order to use it in Fast Fourier transformation of the surface profile data. Test names, wave parameters, duration of the test, and sampling rate used in the irregular wave experiments are listed in Table 4.5.

Table 4.5: Irregular wave tests and parameters used in experimental study

Test Name	Hs [cm]	Tp [s]	Test duration [s]	Wave gauge sampling rate [Hz]
D-H4-T02	9.97	1.94	1790	9.1531
D-H6-T02	17.16	2.38	2190	7.4813
D-H8-T02	21.71	2.77	2530	6.4759
D-H4-T04	9.72	1.37	1270	12.9008
D-H6-T04	17.27	1.78	1550	10.5703
D-H8-T04	20.74	1.96	1790	9.1531

The irregular waves that had been previously researched were assessed in the channel. Both time-dependent statistical wave features and frequency-dependent spectra were evaluated and compared with the spectrum of the theoretical wave using a Python program to process the collected data.

After placing the floating wind turbine model in the channel, all the wave tests listed in Table 4.5 were conducted, and the hydrodynamic performance was investigated by wave measurement, load cell measurement, and video recording for image processing. Surge, heave, and pitch responses under the tests of D-H6-T02 and D-H6-T04 are given as frequency versus power spectral densities (PSD) in Figures 4.12 and 4.13.

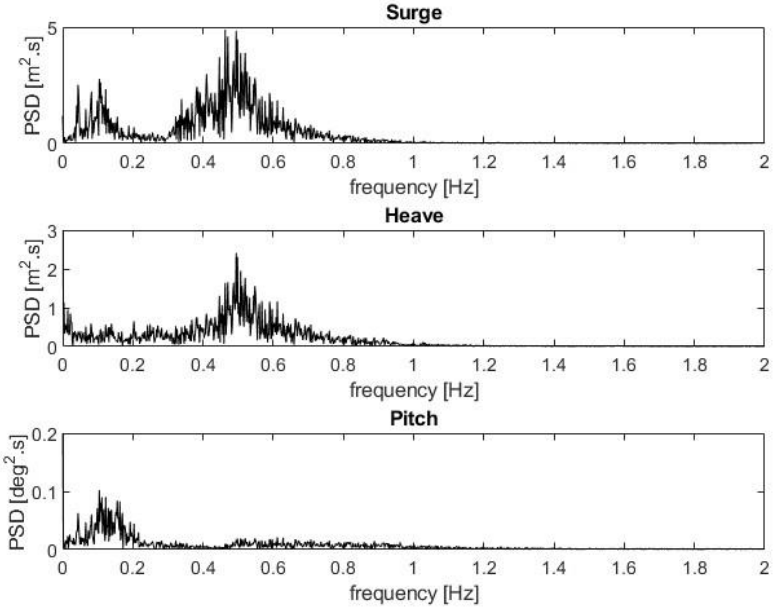

Figure 4.12: PSD of the novel platform under D-H6-T02 irregular wave test

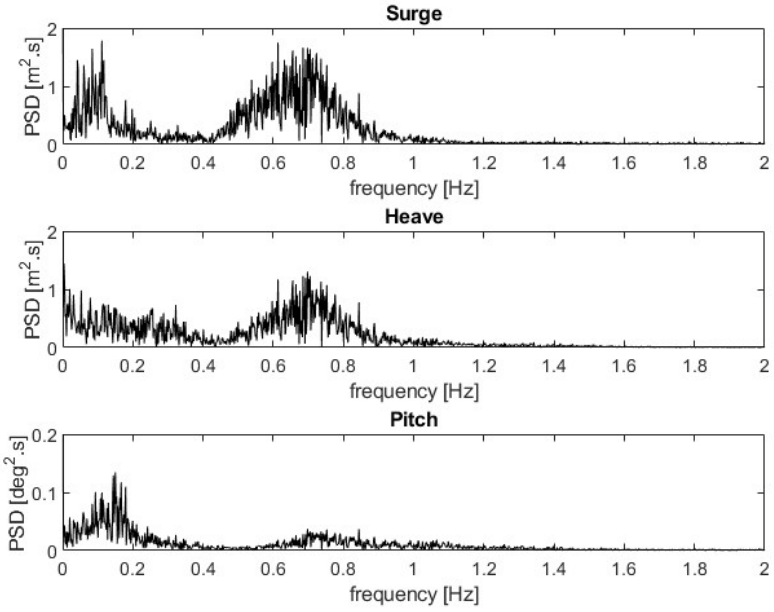

Figure 4.13: PSD of the novel platform under D-H6-T04 irregular wave test

Moreover, Figures 4.14 and 4.15 represent the spectral densities of the tension for the three chains under the tests H6T02 and H6T04.

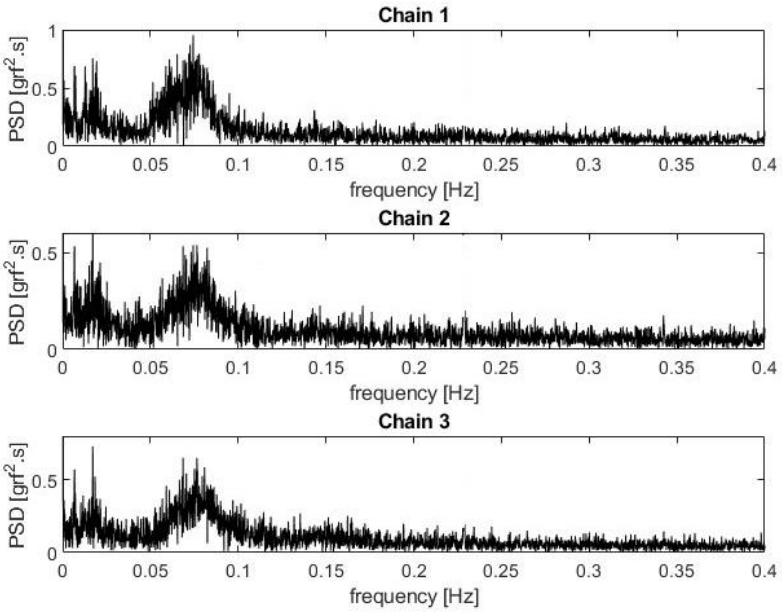

Figure 4.14: PSD of the chain tensions under D-H6-T02 irregular wave test

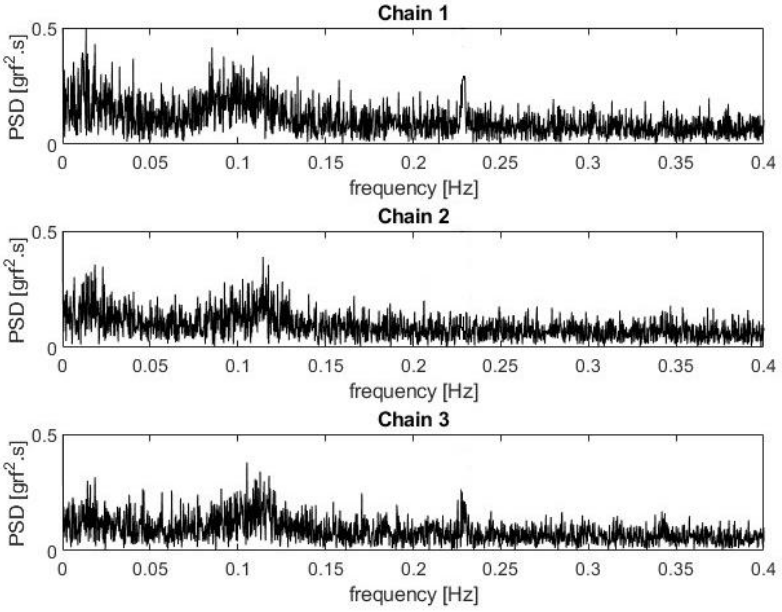

Figure 4.15: PSD of the chain tensions under D-H6-T04 irregular wave test

.

4.6. Irregular Wave and Wind Test

In this section of the study, the irregular wave conditions given in Table 4.5, except DH8-T02 and DH8-T04, were performed under the influence of wind while the tower propeller was also in operation. Surge, heave, and pitch responses under the tests D-H6-T02 and D-H6-T04 are given as PSD in Figures 4.16 and 4.17.

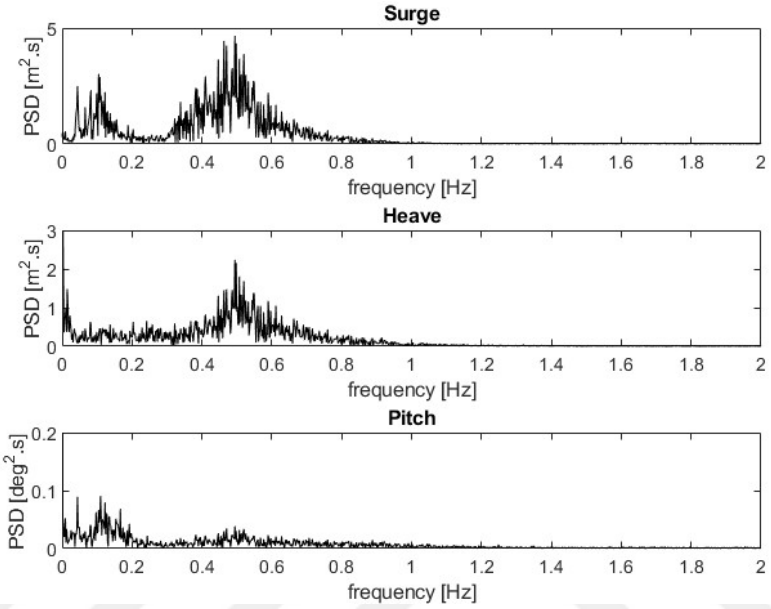

Figure 4.16: PSD of the novel platform under D-H6-T02 irregular wave&wind test

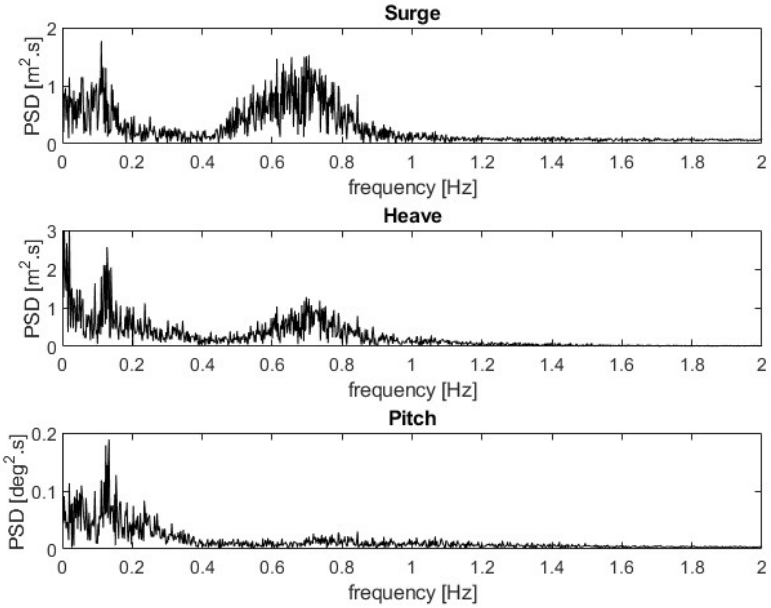

Figure 4.17: PSD of the novel platform under D-H6-T04 irregular wave&wind test

4.7. Comparison of Experimental Results Between Spar Platform and Innovative Platform

In this section, a comparison is made between the experimental results of the novel floating platforms and a spar-type platform, which was previously tested in the IZTECH Hydraulic Laboratory (Aktas, 2020), and a comparison study was performed for three degrees of freedom. Floating wind turbines are subject to displacement and rotation with six degrees of freedom in the real world. However, because the wave in the wave channel in the laboratory is unidirectional, the structure is excited in the surge, heave, and pitch motions; therefore, these three degrees of freedom are the main responses.

4.7.1. Free Decay Tests

Figure 4.18 displays the results of the free decay test for spar and the new platform, whereas Figure 4.19 compares the natural periods of both platforms.

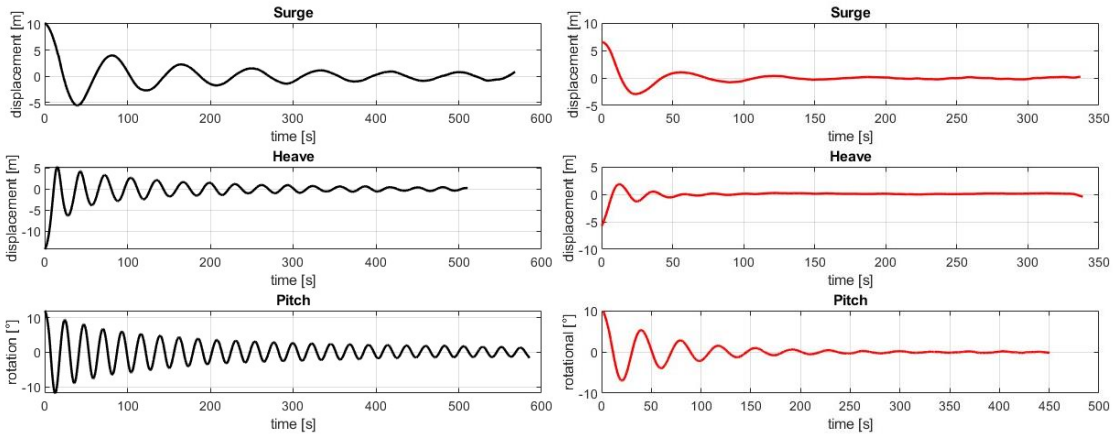

Figure 4.18: Free decay test results for the spar (left) and innovative platform (right)

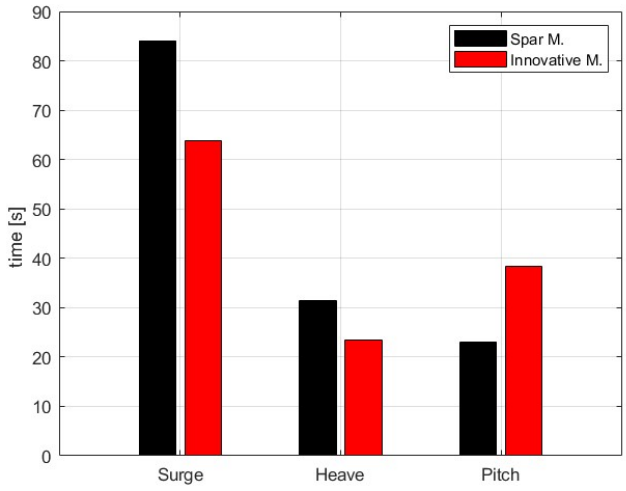

Figure 4.19: Natural period for spar (left) and innovative platform (right)

Figure 4.18 demonstrates that the new platform dampens considerably faster than the spar. As can be seen in Figure 4.19, the natural periods of both platforms are far from the wave period range (20-25 seconds), hence there will be no resonance issues.

4.7.2. Regular Wave Tests

Figure 4.20 compares the spar and the new platform in terms of the displacements and rotations under regular waves.

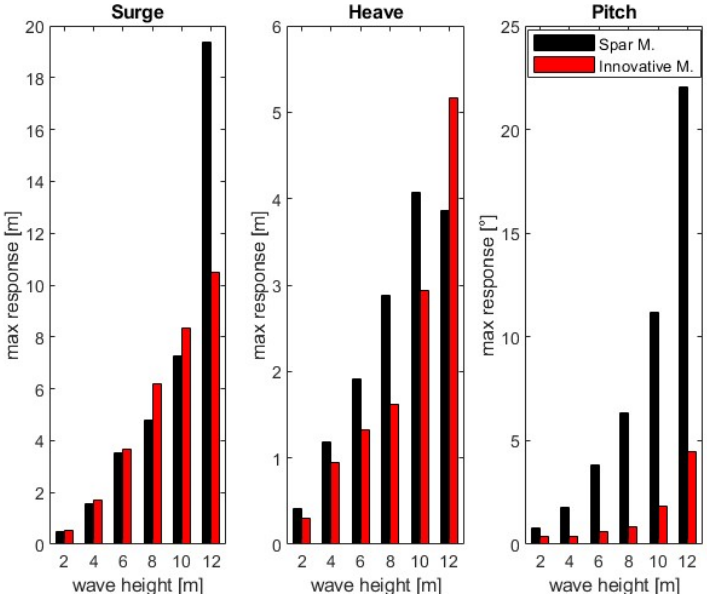

Figure 4.20: Comparison of surge, heave and pitch motions of the spar and the new platform under various wave heights

Figure 4.20 demonstrates that the surge motion is similar for both platforms; however, the heave motions are slightly better for the new platform up to 10 m wave. In the pitch motion, it is evident that the new platform rotates significantly less. This rotation is the most important movement in floating wind turbines in terms of stable energy generation and the resulting fatigue loads. The less the turbine rotates, the more stable it will be and the more stable the energy generation will be.

4.7.3. Regular Wave & Wind Test

In wave and wind experiments, the wave height varied between 2 and 12 meters, while the wind velocity remained constant at 20 m/s. The data illustrate the wave movements that occur after the wind begins to blow. Figure 4.21 demonstrates that when wave and wind interact with a structure, the displacement and rotation of the innovative platform is smaller than the spar platform. Therefore, it has been demonstrated that the novel floating platform is a feasible alternative for offshore wind energy.

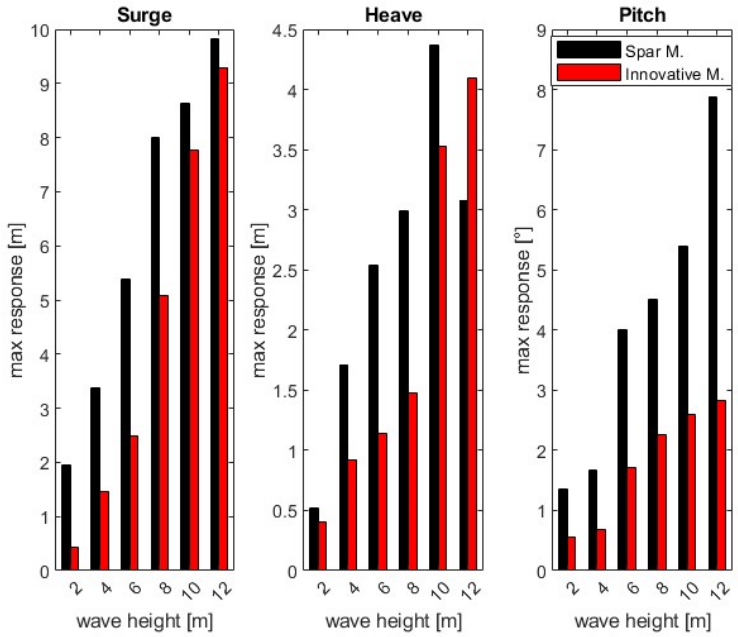

Figure 4.21: Comparison of the surge, heave and pitch motions of the spar and the new platform under the condition of various waves and the extreme wind acting together

CHAPTER 5

CALIBRATION AND VALIDATION OF THE NUMERICAL MODEL

The ANSYS-AQWA hydrodynamic numerical program was used to simulate and analyze the innovative platform, which was equipped with a 300-kW turbine and placed in 40 meters of water. Although ANSYS-AQWA is a known and widely used program for floating bodies, it is necessary to calibrate and verify the numerical model using the experimental test results. In the calibration phase, free decay tests were used, and verification was performed through regular and irregular wave tests. Due to the usage of the 1/40 Froude scale in the experimental model and experimental parameters, the experimental data to be compared with the numerical model results were transformed into prototype l values using scale factors given in Table 3.4.

5.1. Calibration Study

Firstly, the same free decay tests summarized in Table 4.2 were also performed by the numerical model. Then, the free decay test results of both the numerical and experimental models were compared in Figure 5.1 for the surge, heave, and pitch motions.

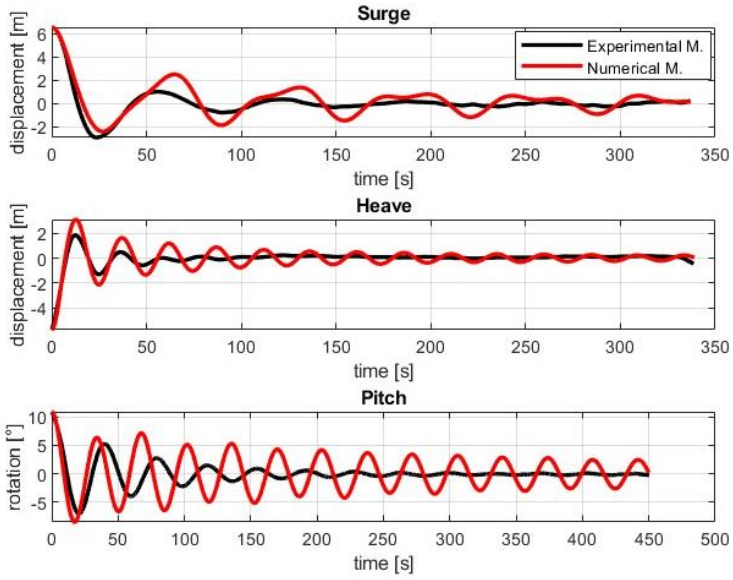

Figure 5.1: Free decay results of the experimental and numerical model before calibration

Figure 5.1 shows that there are discrepancies in the responses between the experimental and numerical models. Therefore, calibration is necessary. For the calibration, the p&q analysis method adopted by Helder and Pietersma (2013) was used.

Figure 5.2 illustrates a usual free-decay motion in the time domain. Φ_n is the amplitude of a decay cycle, and T_Φ is the period of the decay cycle.

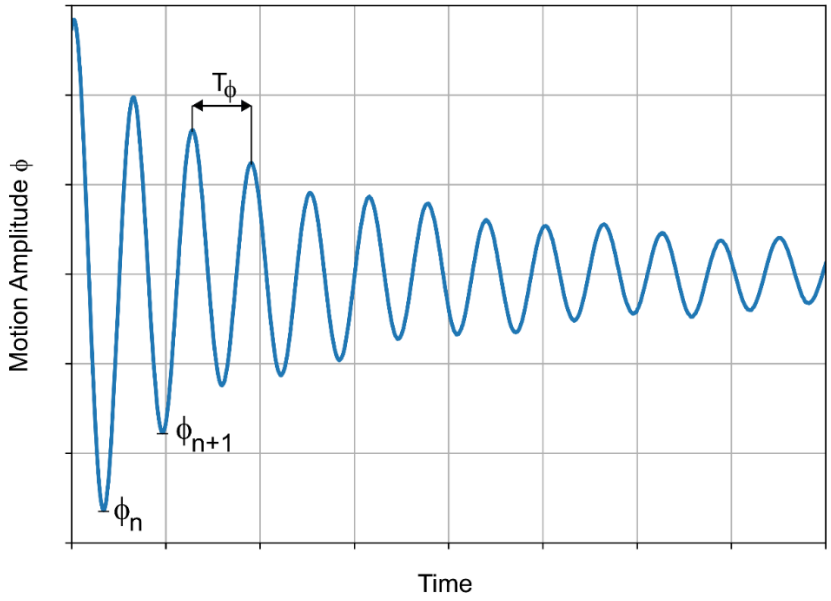

Figure 5.2: Free decay motion in the time-domain

As shown in Figure 5.3, the p&q analysis approach relies on the linear regression analysis of the decay in normalized motion amplitudes relative to the mean motion amplitude. In this method, p represents the y-intercept and q represents the slope of the linear line. They are directly proportional to the signal's linear and quadratic damping.

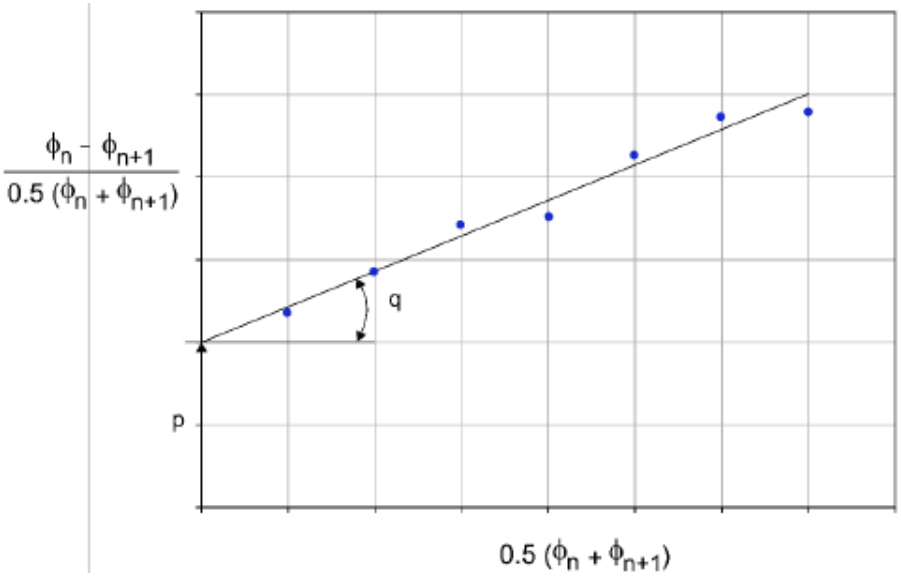

Figure 5.3: p&q analysis schematic

To calibrate the numerical model, the natural period and damping characteristics of the surge, heave, and pitch motions were checked. For the natural period calibration, added mass values of three DoFs were calculated and updated in the numerical model for the damping behavior; the damping coefficient values (linear and quadratic) were adjusted according to p&q analysis till there was a good agreement between the experimental and the numerical FDT results. Figure 5.4 depicts the comparison of free decay test results between the experimental and calibrated numerical models.

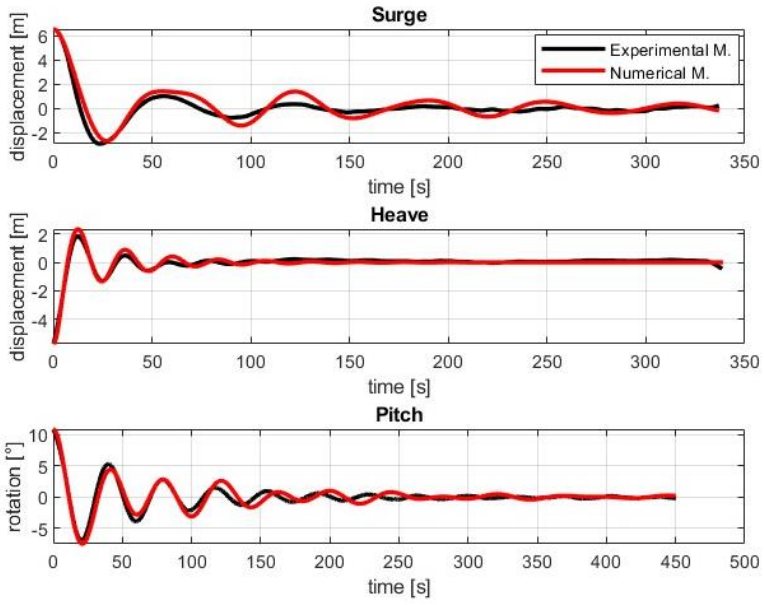

Figure 5.4: Free decay results of experimental and numerical model after calibration

As can be seen in Figure 5.4, there is a good agreement between the experimental and the numerical FDT results.

Figure 5.5 shows the natural period values of the experimental and numerical models for surge, heave, and pitch movements after calibration.

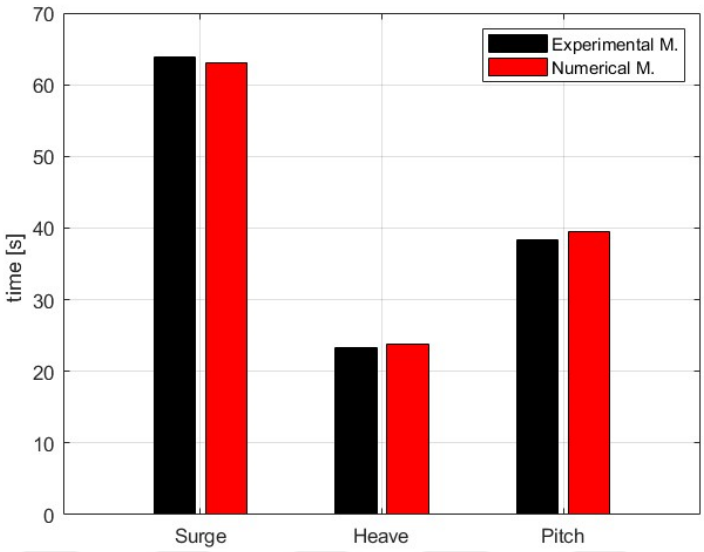

Figure 5.5. Experimental and numerical model results for the natural period

Figure 5.5 shows that the natural periods obtained from the experimental and numercal model are very close to each other.

5.2. Validation Study

5.2.1. Hydrostatic Test

After calibrating the numerical model, an ANSYS-AQWA stability analysis was done without any external forces (wave, wind, current) to test the model's hydrostatic balance. As shown in Table 5.1, the displacements and rotations of the model were close to zero at 6 degrees of freedom following the calibration of the numerical model. This demonstrates that the model is hydrostatically stable.

Table 5.1: Stability results of the calibrated numerical model

Surge (m)	Sway (m)	Heave (m)	Roll (°)	Pitch (°)	Yaw (°)
-2.78E-03	1.13E-02	6.64E-03	-0.11412	-1.18E-02	-0.52953

5.2.2. Quasi-static Tests

For the quasi-static tests, both the experimental and numerical models were used to measure the tension in the chains while the model moved in the positive and negative x directions in still water. Examining the chain tensions of the numerical model and the experimental model for all three chains reveals that the behavior of the posterior chains (Chains 2 & 3) is consistent; however, the behavior of the front chain (Chain 1) is discordant. The reason may be that the high tensions in the experiments exceed the capacity of the load cell connected to the front chain. In future studies, this problem may be overcome by using a load cell with a higher capacity, which allows the collection of more accurate measurements. Figure 5.6 depicts the tension comparisons for the anterior chain, whereas Figure 5.7 depicts the posterior chains.

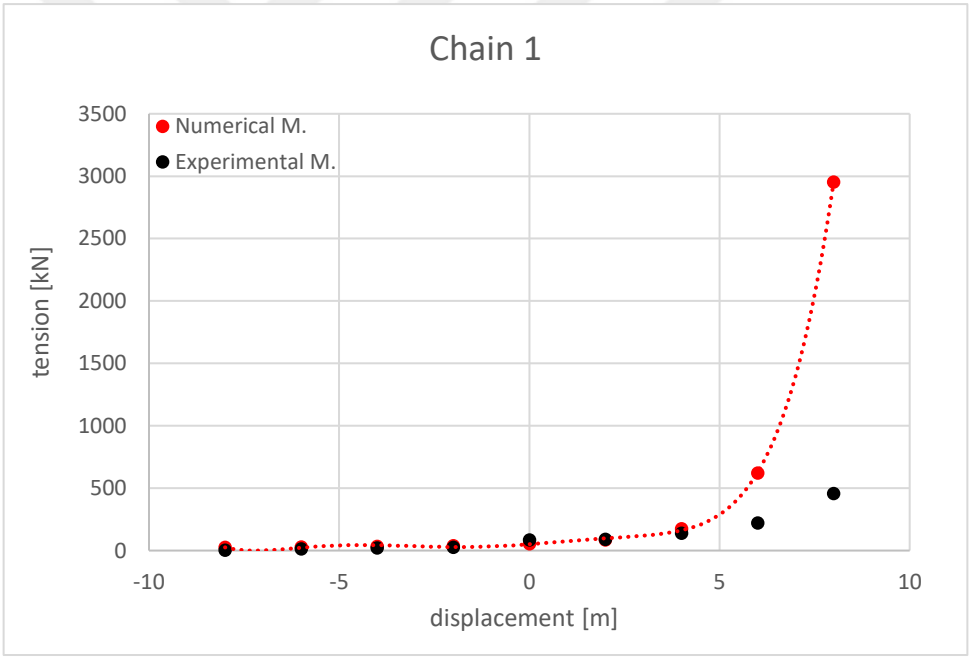

Figure 5.6: Comparison of tensions in the chain 1 between experimental and numerical model

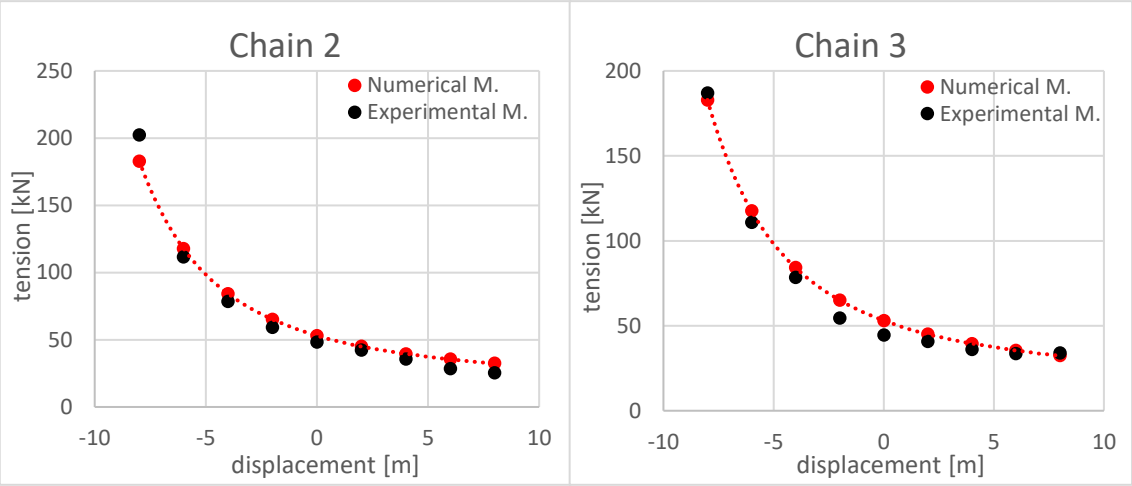

Figure 5.7: Quasi-static test response of chain 2(left) &chain 3(right) for exp. and num. model

5.2.3. Regular Wave Tests

The numerical model was run under the same regular wave conditions produced in the physical model tests (Table 4.3) for validation. The maximum surge, heave, and pitch motions are compared with the experimental results, and the results are shown in Figure 5.8.

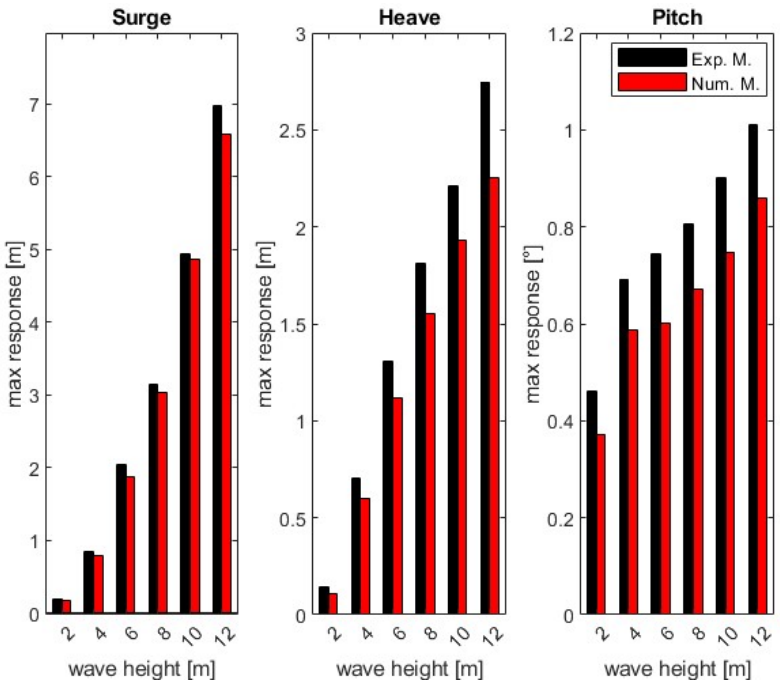

Figure 5.8: Maximum responses of the experimental and the numerical model

As can be seen in Figure 5.8, experimental and numerical model results agree very well for the surge motion. The numerical model results are smaller than the experimental ones for the heave and the pitch. However, it can be stated that the difference is less than 20%, so the agreement is reasonable.

In addition, for each test, the maximum chain tension values obtained from experiments and the numerical model during regular wave tests were compared, and they are shown in Figure 5.9. As can be seen in Figure 5.9, the experimental and numerical model results mostly agree, and there is only a discrepancy between the numerical and experimental model values for chain 1 for an extreme wave with a 12 m height.

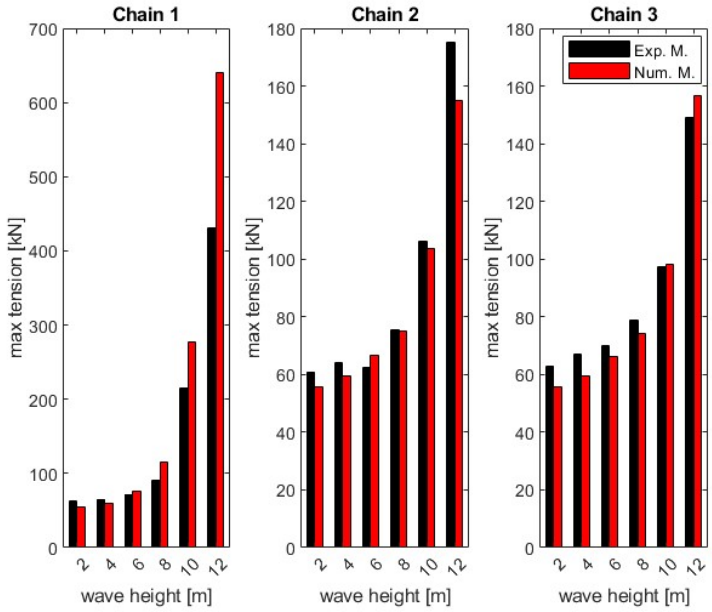

Figure 5.9: Maximum chain tensions of the experimental and the numerical model under regular waves

5.2.4. Regular Wave and Wind Tests

All regular wave experiments were repeated and compared by applying the wind profile to both the experimental model and the numerical model. These comparisons focused on the maximum values of the surge, heave, and pitch motions (Figure 5.10). Although there is a significant increase in both experimental and numerical results during the transition from 8 m to 10 m wave height for the pitch motion, the experimental and numerical model results are, in general, consistent.

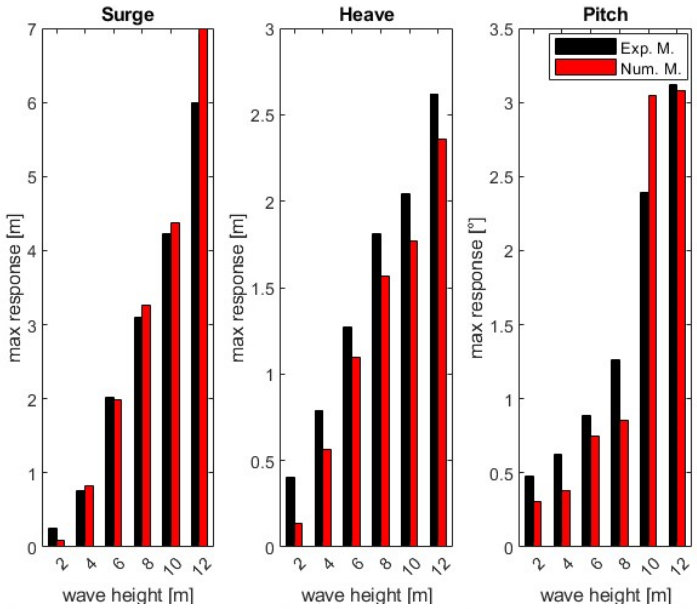

Figure 5.10: Maximum responses of the experimental and the numerical model

In the comparison done for the maximum chain tensions, the numerical model results fit the experimental ones in the posterior chains, and the agreement is better than the anterior chain. Considering the chain tension forces for the numerical and experimental models, while the discrepancy between the numerical and experimental model results increases at wave heights of 10 and 12 m in the posterior chains, a general mismatch is detected in the anterior chain (Figure 5.11).

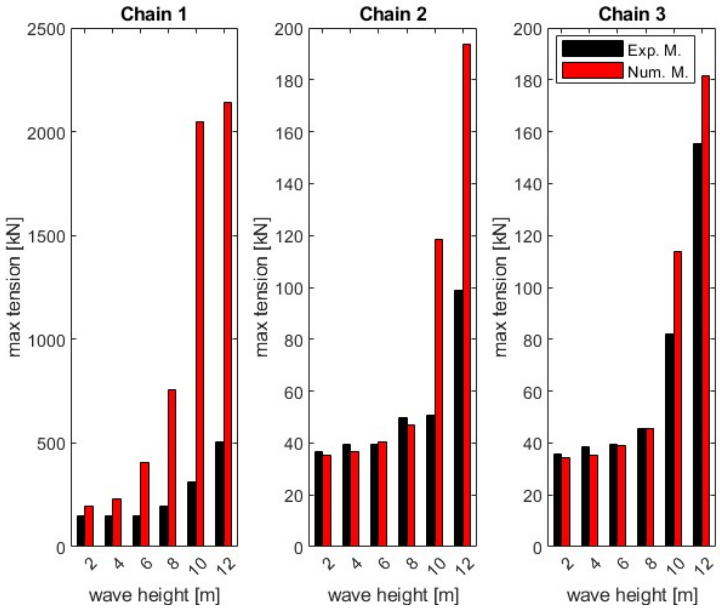

Figure 5.11: Maximum chain tensions of the experimental and the numerical model

5.2.5. Irregular Wave Tests

The numerical model was run under irregular wave test conditions given in Table 4.3. Response results are given as PSD curves in Figure 5.12. As can be observed, the experimental and numerical model responses overlap to a large extent in terms of peak periods and amplitudes.

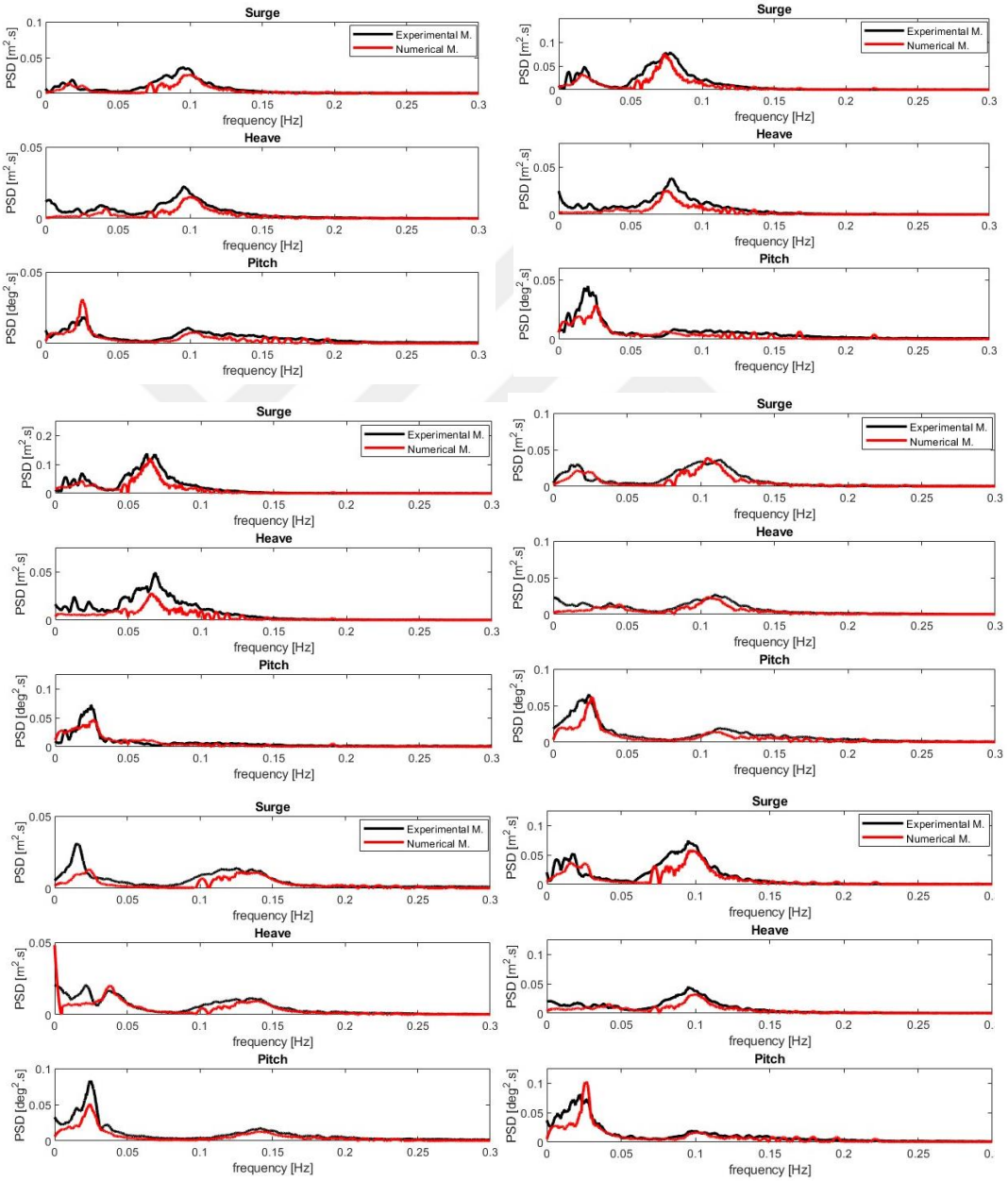

Figure 5.12: PSD of the experimental and the numerical model for irregular wave cases

Figure 5.13 shows the numerical and physical model comparisons for the maximum tensions in the chains. As observed in the regular wave case, numerical and experimental results for the tensile forces in the posterior chains are close; however, the difference for the anterior chain is higher.

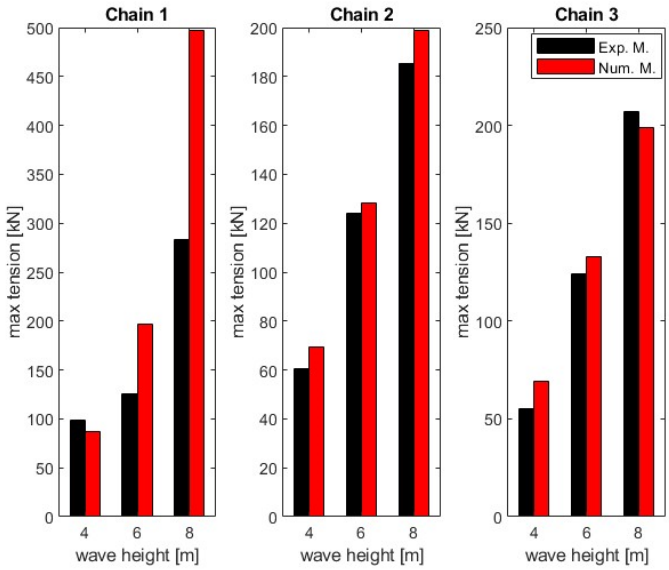

Figure 5.13: Maximum chain tensions of the experimental and the numerical model under irregular waves

5.2.6. Irregular Wave and Wind Test

The numerical model was run under the combination of irregular waves and extreme wind. Figure 5.14 shows the comparison of PSD of the surge, heave, and pitch responses between the numerical and experimental model results.

Furthermore, the bar graph of the maximum tensile forces measured in the chains is compared in Figure 5.15.

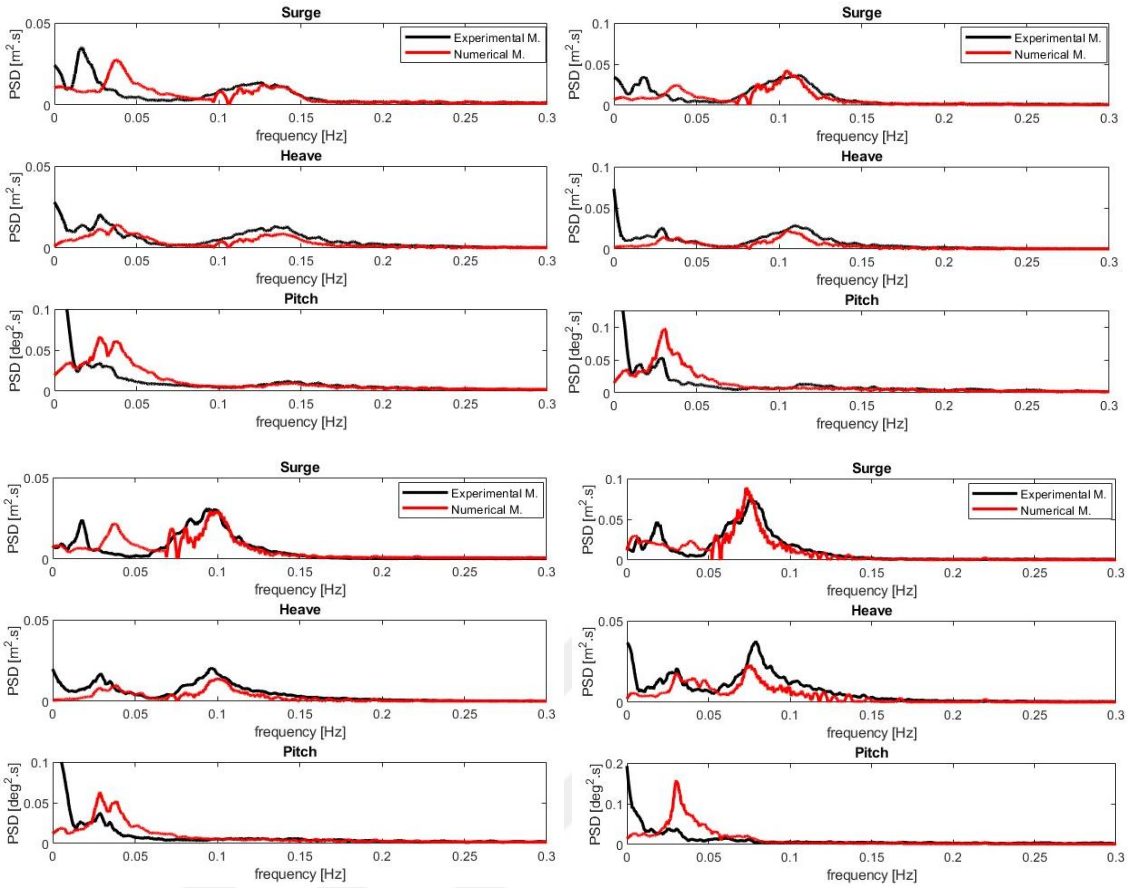

Figure 5.14: PSD of the experimental and the numerical model for irregular wave&wind cases

As can be seen in Figure 5.14 some differences were noticed in pitch movement, although surge and heave were better suited to it.

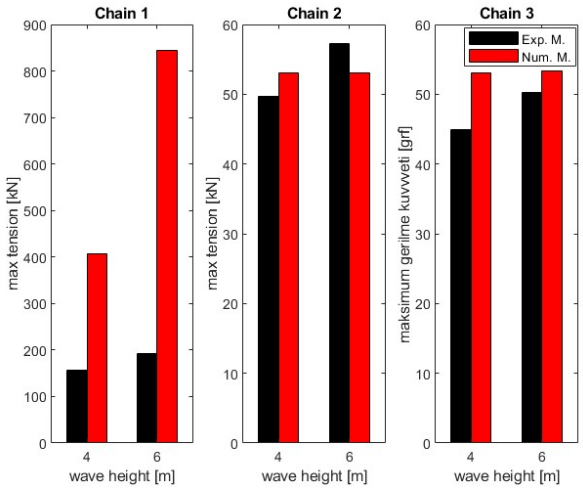

Figure 5.15: Maximum chain tensions of the experimental and the numerical model

Figure 5.15 shows that there is a good agreement in the maximum tensions between the numerical and experimental model results, especially for chains 2 and 3.

CHAPTER 6
CONCLUSIONS

In this study, the hydrodynamic response of a new floating platform for offshore wind turbines developed through two Tübitak projects was examined experimentally and numerically. The following conclusions are drawn:

1) The new platform is examined under extensive test series with various wave and extreme wind conditons, and results show that it is stable, and responses are lower than the required limits.

2) Hydrodynamic responses of the new platform are compared with a well-known spar-type platform through physical model tests under the same wave and wind conditions. Comparison results show that heave and pitch motions, which are critical for producing stable energy under wind and wave conditions, have been reduced in the new platform compared to the spar model. It may be due to the suspended heave plates, and submerged floaters with no water plane area in the novel design.

3) Numerical model developed to examine the hydrodynamic responses of the offshore turbine with the new floating platform is calibrated using free decay test results of the physical model study. After calibration, regular and irregular wave-only tests and wave&wind test results of the physical model study are used for the validation of the numerical model. Agreement between the experimental and the numerical results is good for the surge, heave and pitch responses and the discrepancies are less than 20%. Tension comparisons show a better agreement in the posterior chains (chain-2 and-3) than the chain-1. It may be due to the insufficient capacity of the load cell used in the laboratory tests so that the higher tensions could not be measured in chain-1. However, general agreement in the comparison of the numerical and experimental model results represents that the numerical model can be used to model the prototype of the system and to optimize the geometry increase the performance in the prototype scale.

4) In contrast to the spar, the ballast weight is not positioned in the long draft in the new platform. In fact, the ballast is suspended with chains to the tower. Also, it is planned that the floaters would be made of concrete instead of steel. Therefore, the platform cost may be significantly reduced. However, a thorough cost estimate study is required as a future study.

5) Those extensive tests performed physically and numerically complete the proof of the technology in the lab. The technology readiness level of the platform is 4 due to this study. Demonstration in the relevant sea environment is the next target for the floating platform to bring TRL to 6 as a future study.

6)Structural analysis of the floating platform was out of the scope in this study. However, it is an essential analysis before the demonstration of the system in the relevant sea environment. Therefore, the structural analysis is kept as a future study.

REFERENCES

Aktaş, Kadir. 2020. “Wave Generation and Analysis in the Laboratory Wave Channel to Conduct Experiments on the Numerically Modeled Spar Type Floating Wind Turbine.” M. Sc. – Master’s Degree Program, İzmir Institute of Technology.

Alkarem, Yüksel. 2020. “Numerical Examination of Floating Offshore Wind Turbine and Development of an Innovative Floating Platform Design.”

ANSYS Inc. 2013. “Aqwa Theory Manual” 174.

Anyoji, Masayuki, Taku Nonomura, Hikaru Aono, Akira Oyama, Kozo Fujii, Hiroki Nagai, and Keisuke Asai. 2014. “Computational and Experimental Analysis of a High-Performance Airfoil Under Low-Reynolds-Number Flow Condition.” *Journal of Aircraft* 51:1864-1872. doi: 10.2514/1.C032553.

Arıdıcı, Ali. 2022. “Model Design and Experimental Investigation of Floating Wind Turbine” M. Sc. – Master’s Degree Program, İzmir Institute of Technology.

Bayati, Ilmas, Marco Belloli, Luca Bernini, Hermes Giberti, and Alberto Zasso. 2017. “Scale model technology for floating offshore wind turbines.” *IET Renewable Power Generation* 11. doi: 10.1049/iet-rpg.2016.0956.

Benitz, Maija A., David P. Schmidt, Matthew A. Lackner, Gordon M. Stewart, Jason M. Jonkman, and Amy Robertson. 2015. “Validation of Hydrodynamic Load Models Using CFD for the OC4-DeepCwind Semisubmersible.” In *Volume 9: Ocean Renewable Energy*, V009T09A037. St. John’s, Newfoundland, Canada: ASME. https://doi.org/10.1115/OMAE2015-41045.

Bruun, H. H. 2009. "Hot-Wire Anemometry: Principles and Signal Analysis." Measurement Science and Technology.

Butterfield S, Walt Musial and Jason M. Jonkman. 2007. Engineering Challenges for Floating

Offshore Wind Turbines.

Center for Sustainable Systems, University of Michigan. 2022. “U.S. Renewable Energy Factsheet.” Pub. No. CSS03-12.

Cermelli C, Alexia Aubault, M. Innovation and D. Roddier. 2010. “Qualification of a Semi-Submersible Floating Foundation for Multi- Megawatt Wind Turbines.” OTC-20674-PP.

Crowle, Alan, and Philipp R. Thies 2021. Challenges during installation of floating wind turbines. University of Exeter, College of Engineering, Mathematics and Physical Sciences Renewable Energy Group. http://hdl.handle.net/10871/126969.

Dean, Robert G., and Robert A. Dalrymple 1984. “*Water Wave Mechanics for Engineers and Scientists.*” https://doi.org/10.1029/eo066i024p00490-06.

DNV-GL 2018. “DNVGL-ST-0119 Floating Wind Turbine Structures,” no. July: 162.

Erol, Serkan. 2020. “Scaled down modelling of a horizontal wind turbine for a floating wind turbine research”. M. Sc. – Master’s Degree Program, İzmir Institute of Technology. https://hdl.handle.net/11147/10960

GWEC. 2022. “Global Wind Report 2022” GWEC Global Wind Energy Council.

Hasselmann, Klaus. 1973. “Measurements of Wind-Wave Growth and Swell Decay during the Joint North Sea Wave Project (JONSWAP).” *Deutches Hydrographisches Institut*, no. Ergänzungsheft 8-12.

Hedberg, Fredrik and Michael Sacculo. 2014. “Design of a numerical model to analyse a wave energy dissipation device for hydropower.” M. Sc. – Master’s Degree Program, Chalmers University of Technology.

Helder, Joop, and Mario Pietersma. 2013. “Umaine–Deepcwind/Oc4 Semi Floating Wind Turbine Repeat Tests.” *MARIN, Wageningen, The Netherlands*.

Hughes, Steven A. 1993. “*Physical Models and Laboratory Techniques in Coastal Engineering*. *Advanced Series on Ocean Engineering*.” Vol. Volume 7. WORLD SCIENTIFIC. https://doi.org/doi:10.1142/2154.

Jonkman, Jason M., and M. L. Jr. Buhl. 2005. “FAST User’s Guide - Updated August 2005.” https://doi.org/10.2172/15020796.

Jonkman, Jason M. 2007. “Dynamics Modeling and Loads Analysis of an Offshore Floating Wind Turbine” 8 (11): 1595–1606. https://doi.org/10.4161/hv.21225.

Jonkman, Jason M. 2009. Dynamics of Offshore Floating Wind Turbines – Model Development and Verification, (June), 459–492. doi:10.1002/we.

Jonkman, Jason M. 2010. "Definition of the Floating System for Phase IV of OC3." *Contract* 1 (May): 31. https://doi.org/10.2172/979456.

Jonkman, Jason M. and Walt Musial. 2010. Offshore code comparison collaboration (OC3) for IEA task 23 offshore wind technology and deployment. IEA Task 23 303, 74. https://doi.org/NREL/TP-5000-48191

Jonkman, Jason M., Torben Juul Larsen, A. Craig Hansen, Tor Anders Nygaard, K. Maus, M. Karimirad, Z. Gao, et al. 2010. "Offshore Code Comparison Collaboration within IEA Wind Task 23: Phase IV Results Regarding Floating Wind Turbine Modeling." *European Offshore Wind Conference*, April, 23. https://doi.org/10.1007/s00374-009-0370-2.

Jonkman, Jason M., and Denis Matha. 2013. "Dynamics of Offshore Floating Wind Turbines—Analysis of Three Concepts†." *Wind Energy*, no. January: 1–20. https://doi.org/10.1002/we.

Karimi, M., Hall, M., Buckham, B., Crawford, C. 2016. "A multi-objective design optimization approach for floating offshore wind turbine support structures." *J. Ocean Eng. Mar. Energy* (2017) 3:69–87

Kimball, Richard, Andrew J. Goupee, Matthew J. Fowler, Erik-Jan Jan De Ridder, and Joop Helder. 2014. "Wind/Wave Basin Verification of a Performance-Matched Scale-Model Wind Turbine on a Floating Offshore Wind Turbine Platform." In *Proceedings of the ASME 2014 33rd International Conference on Ocean, Offshore and Arctic Engineering*, 9B:1–10. American Society of Mechanical Engineers. https://doi.org/10.1115/OMAE2014-24166.

Li, L., Yan Gao, Zhiqiang Q. Hu, Zhiming M. Yuan, Sandy Day., Haoran R. Li. 2018. "Model test research of a semisubmersible floating wind turbine with an improved deficient thrust force correction approach." *Renew. Energy* 119, 95–105.

Martin, Heather. 2011. "Development of a Scale Model Wind Turbine for Testing of Offshore Floating Wind Turbine Systems."

Mehta, R. D. and Bradshaw, P. 1979. “Desing Rules for Small Low Speed Wind Tunnels,” Aeronautical Journal of the Royal Aeronautical Society, Vol. 73, pp. 443-449.

McCormick, Michael. E. 2010. *Ocean Engineering Mechanics - with applications.* New York City, U.S.A: Cambridge University Press, copyright granted on 2014-08-26.

Moné, Christopher, Maureen Hand, Mark Bolinger, Joseph Rand, Donna Heimiller, Jonathan Ho. 2015. “Cost of Wind Energy Review (Technical Report).” NREL/TP-6A20-66861. National Renewable Energy Laboratory (NREL), Golden, CO (US), Overview, (October).

Musial Walt, Butterfield S and Boone A. 2004. Feasibility of Floating Platform Systems for Wind Turbines Preprint, (November 2003).

OREAC. 2018. High Level Panel for a Sustainable Ocean Economy.

Özbahçeci, Bergüzar. 2004. “Effect of wave grouping, spectral shape and exreme waves in a wave train on the stability of rubble mound breakwaters,” Ph.D. - Doctoral Program, Middle East Technical University.

Özkol, Ünver, Bergüzar Özbahçeci, Sercan Acarer, Timuçin Eriş. 2022. “Yüzer Rüzgâr Türbini Salınım Dinamiği ve Performansının Deniz Dalgaları ve Aşırı Rüzgar Hızları Altında İncelenmesi.” Tübitak 1001 Projesi, no:217M451.

Robertson, Amy. 2015. “Introduction to the OC5 Project.” *EERA Deepwind*, 23. http://www.sintef.no/Projectweb/Deepwind_2015/Presentations/.

Robertson, Amy, et al., 2016. OC5 project phase ib: validation of hydrodynamic loading on a Fixed,Flexible cylinder for offshore wind applications. Energy Proc. 94, 82–101. https://doi.org/10.1016/j.egypro.2016.09.201.

Robinson Mike and Walt Musial. 2006. “Offshore Wind Technology Overview”. U.S. Department of Energy, Energy Efficiency and Renewable Energy. NREL/PR-500-40462.

Sant, Tonio and Kurt Cuschieri. 2016. Comparing Three Aerodynamic Models for Predicting The Thrust and Power Characteristics of Yawed Floating Wind Turbine Rotors. Journal of Solar Energy Engineering. 138. 10.1115/1.4032684.

Sclavounos, Paul D., S. Lee, J. DiPietro, G. Potenza, P. Caramuscio, and G. De Michele. 2010. “Floating Offshore Wind Turbines: Tension Leg Platform and Taught Leg Buoy Concepts Supporting 3–5 Mw Wind Turbines.” In *European Wind Energy Conference (EWEC)*, 3:1–7. https://doi.org/10.1108/IJCHM-08-2013-0350.

Tran, Thanh Toan, and Dong Hyun Kim. 2018. “A CFD Study of Coupled Aerodynamic-Hydrodynamic Loads on a Semisubmersible Floating Offshore Wind Turbine.” *Wind Energy* 21 (1): 70–85. https://doi.org/10.1002/we.2145.

Utsunomiya, Tomoaki, Hidekazu Matsukuma, Shintaro Minoura, Kiyohiko Ko, Hideki Hamamura, Osamu Kobayashi, Iku Sato, Yoshihisa Nomoto, Kentaro Yasui. 2010. “On sea experiment of a hybrid SPAR for floating offshore wind turbine using 1/10 scale model.” In: Proc. ASME 2010 29th International Conference on Ocean, *Offshore and Arctic Engineering*, pp. 529–536.

Utsunomiya, Tomoaki, Eitaro Nishida, Iku Sato, I. 2009b. “Wave response experiment on SPAR-type floating bodies for offshore wind turbine.” In: Proceedings of the Nineteenth (2009) International Offshore and Polar Engineering Conference, pp. 378–383.

Utsunomiya, Tomoaki, Iku Sato, T., Hidekazu Matsukuma, Kiyokazu Yago. 2009a. “Experimental validation for motion of a SPAR-type floating offshore wind turbine using 1/22.5 scale model.” In: Proc. ASME 2009 28th International Conference on Ocean, *Offshore and Arctic Engineering*, pp. 951–959.

Yang,Yang, Musa Bashir, Constantine Michailides, Chun Li, Jin Wang, 2020. Development and application of an aero-hydro-servo-elastic coupling framework for analysis of floating offshore wind turbines. Renew. Energy 161, 606–625.

Yang, Ray-Yeng, Chuan-Wen Wang, Chin-Cheng Huang, Cheng-Hsien Chung, C., Chung-Pang Chen, Chih-Jung Huang, C. 2022. “The 1:20 scaled hydraulic model test and field experiment of barge-type floating offshore wind turbine system.” *Ocean Engineering* 247.110486.